RICE UNIVERSITY

Nonlinear Aeroelastic Analysis of UAVs: Deterministic and Stochastic Approaches
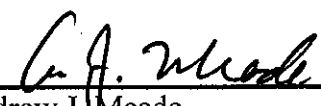
By

Thomas Woodrow Sukut, 2d Lt USAF

A THESIS SUBMITTED
IN PARTIAL FULFILLMENT OF THE
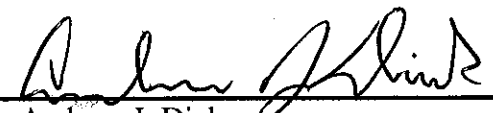REQUIREMENTS FOR THE DEGREE

Master of Science

APPROVED, THESIS COMMITTEE

Dr. Pol D. Spanos, Chair
Lewis B. Ryon Professor of Mechanical
Engineering and Materials Science

Dr. Andrew J. Meade
Professor, Mechanical Engineering
Department Chair

Dr. Andrew J. Dick
Assistant Professor

HOUSTON, TEXAS
April 2012

ABSTRACT

Nonlinear Aeroelastic Analysis of UAVs: Deterministic and Stochastic Approaches

By

Thomas Woodrow Sukut, 2d Lt USAF

Aeroelastic aspects of unmanned aerial vehicles (UAVs) is analyzed by treatment of a typical section containing geometrical nonlinearities. Equations of motion are derived and numerical integration of these equations subject to quasi-steady aerodynamic forcing is performed. Model properties are tailored to a high-altitude long-endurance unmanned aircraft. Harmonic balance approximation is employed based on the steady-state oscillatory response of the aerodynamic forcing. Comparisons are made between time integration results and harmonic balance approximation. Close agreement between forcing and displacement oscillatory frequencies is found. Amplitude agreement is off by a considerable margin. Additionally, stochastic forcing effects are examined. Turbulent flow velocities generated from the von Karman spectrum are applied to the same nonlinear structural model. Similar qualitative behavior is found between quasi-steady and stochastic forcing models illustrating the importance of considering the non-steady nature of atmospheric turbulence when operating near critical flutter velocity.

Acknowledgments

I would like to thank several individuals for contributions to my work here at Rice University. First and foremost I would like to thank Dr. Pol Spanos for giving me the opportunity to work under his advisement. His robust mentorship in class and in various stages of development of this thesis was invaluable.

I would also like to thank my fellow Air Force colleagues for their varied support, especially Matt Guertin and Tony Puntel. Thanks for checking my calculations, helping me debug my code, and tearing me away from the computer every now and then to relax and live a little. Lots of luck in your Air Force careers.

Finally I would like to thank my family and friends for their support up to this point in my personal and professional life. I could not have done it without them. Their love and support has helped me achieve a long list of achievements. I'm proud to now add this master's thesis to that list.

Disclaimer

The views expressed in this article are those of the author and do not reflect the official policy or position of the United States Air Force, Department of Defense, or the U.S.

Contents

List of Figures

List of Tables

Nomenclature

UAV	Unmanned Aerial Vehicle
HALE	High-Altitude, Long-Endurance
DOF	Degree of Freedom
LCO	Limit Cycle Oscillation
h	Plunge displacement
α	Pitch displacement
m	Mass
EA	Elastic Axis
AC	Aerodynamic Center
CG	Center of Gravity
I_{EA}	Moment of inertia about the elastic axis
x_α	Non-dimensional distance between EA and CG
x_β	Distance between EA and AC
c	Chord length
b	Semi-chord length
l	Span length
a	Non-dimensional location of EA
EI, GJ	Flexural and Torsional Rigidity
K_h, K_α	Stiffness coefficients (plunge and pitch)
C_h, C_α	Damping coefficients (plunge and pitch)
L	Aerodynamic lift force
M	Aerodynamic moment
C_{L_α}	Lift curve slope
C_L, C_M	Force coefficients (lift and moment)
ρ	Air density
V	Air velocity

Chapter 1

Introduction

1.1. Motivation

Aircraft offer seemingly endless technological possibilities, yet in order to fully take advantage of them it is necessary to have a complete understanding of every process involved. In the century since man's first flight, understanding the mechanisms responsible for such a feat has been a major priority. Basic aerodynamics, structural considerations, navigation techniques, and control systems have all evolved around the goal of taking advantage of our atmosphere. As technology advances more questions have been raised which have continued to fuel man's quest for answers. Modern research is concerned less with how to get an aircraft to fly than with how to get it to fly better; how can the boundaries of possibility be expanded?

One of the major challenges facing aircraft designers today is that of aeroelasticity. Complex interactions between dynamics, solid mechanics, and aerodynamic forces can create problems if not well understood and analyzed. Aircraft structural fatigue, passenger discomfort, decreased performance, and even catastrophic failure can result. Early in the history of the airplane this problem was minimal due to low flight speeds, large factors of safety, and moderate performance requirements. Today's aircraft, however, are expected to push the physical limits in terms of speed, altitude, maneuverability, endurance, range, and cost. Designers are turning to lightweight materials for use with high-powered engines to reduce weight in order to carry more fuel and payload. These lightweight materials exhibit more flexibility than conventional aircraft materials which when used at higher speeds and altitudes pose possible aeroelastic concerns. With current computational resources it is becoming more feasible to model and correct for aeroelastic deficiencies, yet advancements in the theory and practice of aeroelastic analysis fail to match the pace of performance requirements. Thus further innovation is inhibited until the phenomenon of aeroelasticity can be fully understood.

In the preceding direction, this work aims to break down aeroelastic phenomenon into its basic components, apply current techniques to generate a detailed structural model, and then use various nonlinear methods to analyze said model in the aeroelastic framework. The end goal of this work is to weigh the feasibility, effectiveness, and cost of the various analysis methods. Though generally applicable to most aircraft designs, for the purposes of this thesis the analysis will

be carried out in the context of a typical high-altitude, long-endurance (HALE) unmanned aerial vehicle (UAV).

1.2. Aeroelasticity Explained

The term aeroelasticity is used to refer to any phenomena in which inertial, aerodynamic, and elastic forces interact [1]. These interactions can be as inconsequential as a slight vibration, and as catastrophic as a complete structural failure. Aeroelastic analysis encompasses the fields of dynamics, structural mechanics, and aerodynamics, and they all hold equal importance. Aeroelasticity can refer to numerous structural/aerodynamic interactions such as wind interactions with power lines, suspension bridges, and buildings. For the purposes of this thesis, however, aeroelastic analysis will be focused on the behavior of an aircraft wing in an air stream. In aircraft aeroelasticity, aerodynamic forces on flexible bodies (wings, control surfaces, etc.) produce displacements that cause the body to interact with the air around it. Inertial forces are encountered, as well as changes in the aerodynamic forces based on the changing incidence of the body with the airflow. These additional forces produce additional displacements which, in turn, produce additional changes in the forces. As no structure is completely rigid, certain manifestations of this phenomenon is expected in all aircraft. However, the rigidity and structural damping of the aircraft wing should be such that this phenomenon is minimal or nonexistent during normal operation. For instance, if an aircraft wing is disturbed, perhaps through a wind gust, the desired behavior is that the wing stiffness and damping along with the aerodynamic and inertial interactions

should work to quickly return the wing to a stable equilibrium. If the disturbance is instead maintained or amplified through the structural, aerodynamic, and inertial interactions, the behavior can possibly result in material fatigue and ultimately structural failure. The main design tradeoff which affects aeroelasticity is weight versus wing stiffness. Strong stiff wings weigh more, require more fuel, and do not permit as much payload, but they are less likely to encounter aeroelastic interactions. To prevent the reduced efficiency from heavier wings, stiffness is usually sacrificed for lighter weight components which tend to be more flexible and therefore more prone to aeroelastic interactions.

Aeroelasticity can be broken into two main categories: static and dynamic. Cases in which the inertial forces play a negligible role are referred to as static. In static aeroelasticity, the aerodynamic forces are simply greater than the elastic restoring forces [2]. The resulting instability is called divergence and if not detected and corrected quickly, can be catastrophic. Dynamic aeroelasticity involves influential inertial forces and the associated instabilities are referred to as flutter [2]. As Reference [3] describes, when a cantilever wing is disturbed, the wing oscillates about its equilibrium until eventually the oscillations damp out. If the same wing is subjected to an airflow the damping effect increases as the flow velocity increases to a certain point. After this point, however, further increases in the flow velocity result in a rapid decrease in the damping. The point at which the damping reaches zero and sustained oscillations are possible is called the critical flutter velocity. By further increasing the flow velocity the wing enters a phase of

negative damping in which even minute disturbances can result in large violent oscillations. These oscillations can have both bending and torsional components.

Flutter is often thought of as a resonance problem. In reality, flutter is a self-excited phenomenon. Reference [4] describes the mechanism responsible for flutter as a coalescence of the natural frequencies of the structure. When the frequencies approach each other the airfoil extracts energy from the airstream which results in oscillations. This behavior is shown in Figure 1-1. At point A the frequencies are distinct, no energy extraction occurs, and the system damping causes the amplitude to decrease. At point B the frequencies have approached each other such that disturbances result in harmonic oscillations with constant amplitude. Point C demonstrates the coalescence of the frequencies and the introduction of flutter [4]. In the linear case this behavior will continue to grow in amplitude until wing failure. In the nonlinear case various mechanisms can result in limit cycle oscillations (LCO).
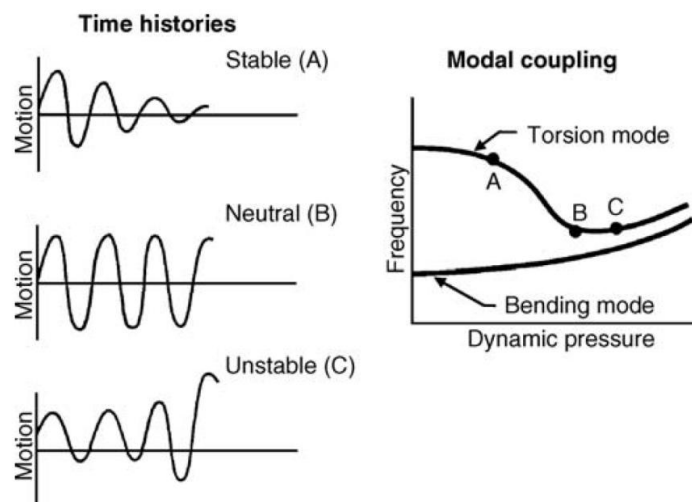
Figure 1-1: Coalescence of Vibration Modes [4]

From this description one can see that aircraft flutter is generally experienced as a high frequency oscillation of the wing. Adequate control systems can be developed to correct for this behavior. However, to precisely control the aeroelastic behavior for a particular aircraft design the behavior must first be modeled accurately for the control system to be effective. The high frequency of the oscillations does not permit proper human compensation in most cases [1]. Divergence and flutter can both be encountered suddenly and without warning. The role of aeroelastic analysis is to predict the operational conditions which might permit such behavior, so that these conditions can be avoided entirely either through design accommodations or operational limitations.

Another aspect of aeroelasticity is that of aileron reversal. This phenomenon occurs at certain flight conditions where by increasing the velocity the aileron effectiveness decreases to zero and then becomes negative [2]. Though not generally catastrophic in itself, consequences of this behavior can lead to failure and ineffective aircraft handling. For example, if one attempts to reduce loading on a wing, the result may actually be an increased loading on the wing if the ailerons have reversed. Overloading the wing can then lead to fatigue and failure. Though this thesis does not explicitly address aileron reversal, it is mentioned herein as a possible source of excitation that can lead to static and dynamic aeroelastic behavior and one that any aircraft operator should be aware of.

1.3. Past and Present Research

Aeroelasticity issues have been encountered since the birth of the airplane. Widely known as the "first in flight," the Wright brothers' successful airplane was actually almost beaten by a competitor. Professor Samuel P. Langley's first flight was only a few days before the Wright brothers'. Langley's flight, however, was not successful and its failure is widely attributed to wing torsional divergence [1]. Langley's monoplane design lacked the necessary torsional rigidity to accommodate the applied aerodynamic moment and the plane crashed into the Potomac River after the wing failed. The Wright Flyer, on the other hand, used a biplane design that employed "wing warping" for lateral control. This enabled the pilot to control the craft without drastically altering the wing characteristics [2]. The biplane design featured twin wings reinforced with cables between them. The result was much higher torsional rigidity than a comparable monoplane before successful "stressed skin" designs were later realized in the 1930s [2]. Because of the success of the Wright Flyer and failure of Langley's plane, designers opted for the proven biplane design. Had the Wright Flyer not been successful, perhaps early aircraft designers might have sooner understood the necessary torsional requirements necessary for monoplanes.

As most early aircraft designs were based on the successful biplane, the first major aeroelastic issues encountered involved tail flutter [1]. At the beginning of World War I pilots of the Handley Page 0/400 bomber experienced violent oscillations of the fuselage and tail. In what is often cited as the first documented

investigation into the flutter problem, the investigators found that the aircraft had two principal modes of vibration [1]. One mode involved torsional oscillations of the fuselage, while the other mode caused the left and right horizontal tail surfaces to oscillate 180° out of phase. Coupling between these two modes was possible which resulted in the violent oscillations that were experienced. The solution to this was to connect the left and right horizontal tail sections to the same torque tube to prevent the second mode from occurring [1].

The importance of aeroelastic considerations with respect to wings was not readily apparent until later during the war with the development of the Fokker D-8 high performance monoplane. [1]. Static tests showed the wing able to withstand adequate design load factors, but it was found that as the aerodynamic load increased, the angle of attack at the wing tips increased more than at the wing root meaning the wings were experiencing excess tip loading which led to structural failure [1]. Other aircraft designs of the time were also beginning to push the limits of technology and understanding. Increased flight speeds exerted increased aerodynamic loads which the structures were not designed to handle properly in dynamic situations. Numerous aircraft losses and the prospect of losing a competitive military advantage resulted in the first serious research efforts to understand and fix the root causes of aeroelasticity. Unfortunately, designers were unable to understand or simply did not trust many of the theories put forth in the 1920s and 1930s [1].

In analyzing aeroelastic problems, linear techniques can be quite insightful. However, their applicability to real-world nonlinear problems is limited. Linear analysis techniques can help predict the speed at which flutter or divergence might occur, but may not be useful for determining the speeds at which a real-world nonlinear system might develop self-excited oscillations [2]. Linear analysis techniques also cannot predict the effects of small perturbations which might result in an oscillatory response. These self-excited or perturbed oscillations can lead to what is called limit cycle oscillations (LCO). LCO are steady-state oscillations which pose long-term fatigue problems and can affect passenger comfort and pilot endurance [2]. Cyclical loading and unloading can cause material deterioration and the formation of small cracks. While the loading may not exceed the failure limits of the material, repeated cyclic loading can eventually lead to failure due to fatigue [5]. With modern computational capabilities, nonlinear analysis techniques are able to address these problems, though they are still quite expensive in terms of both computational resources and time.

In order to understand the complex interactions, researchers have broken aeroelasticity down into several subsets. Figure 1-2 shows the three major subsets as well as their interactions to form intermediate fields of study which are also pertinent to the subject at hand. The aeroelastician must be well versed in the fields of dynamics, solid mechanics, and unsteady aerodynamics. Several well known texts are available detailing the progress in aeroelastic analysis. For additional information the reader is referred to References [1], [2], [3], and [6], among others.
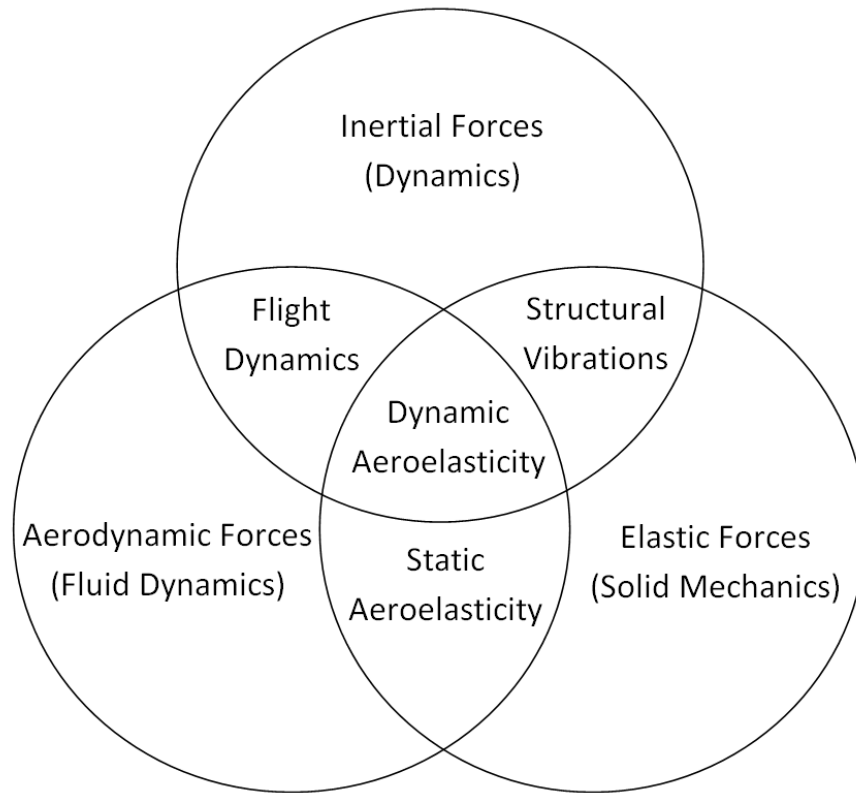
Figure 1-2: Components of Aeroelastic Analysis [6]

The research community has made great strides in modeling and

understanding aeroelastic phenomena, yet no complete grasp of the complexities

involved has been achieved. A great deal of aeroelastic analysis is reactive in that it

focuses on analyzing preliminary aircraft designs for any potential problems. To this

end many researchers are focused on accurately modeling the aerodynamic

environment and structural components of the design while maintaining

computational efficiency. Reference [7] presents a detailed computational

aeroelastic analysis of an aircraft using a finite element structural model coupled to

an aeroelastic analysis code. Computational analysis models are very common in

recent literature. References [8], [9], [10], [11], and [12] are just a sample of all the various papers available. From these references, it is apparent that there are many ways to model and analyze aeroelastic phenomena. Models range from simple linear single degree of freedom structural models excited by simple linear aerodynamic models, to fully nonlinear finite element models coupled to complete unsteady aerodynamic codes. Each approach has advantages and disadvantages, and each offers insights into the mechanism of aeroelasticity. The broader perspective is that although aeroelasticity is not completely understood. The problem can be modeled and analyzed for use in aircraft design and operations by making various assumptions. One ultimate goal is to make aeroelastic considerations proactive, where certain performance characteristics can be incorporated that take advantage of the aeroelastic interactions.

1.4. Application to UAVs

UAVs are aerial vehicles designed to perform tasks which traditionally require a manned vehicle. Typical UAV configurations are either fixed wing or rotary wing and can range from several inches to hundreds of feet long [13]. Their missions are as varied as their configurations as well. UAVs have been designed for weather and atmospheric research, reconnaissance and surveillance, conventional combat, remote sensing, mapping, traffic monitoring, and search and rescue to name a few [13], [14]. Though no universal UAV classification exists, by convention UAVs are grouped according to size, weight, and capabilities. The vast majority of UAVs fall into one of three different categories. The first category covers most UAVs which

consist of conventional aircraft designs used for low altitudes and relatively short durations. The second category covers high altitude and long duration missions. The third category includes unconventional designs and those with special launch and recovery modes [15]. Table 1-1 shows some general UAV classifications and characteristics.

Table 1-1: General UAV Classifications and Characteristics [16]

Tactical UAV	Ubiquitous 50 to 1000 lb deployable air vehicle
Endurance UAV	Capable of extended missions, typically 24 hours or longer
Vertical Takeoff & Landing (VTOL)	Typically rotary wing UAV
Man Portable UAV	Being light enough to be back-packed by an individual and launched by hand-throwing or sling-shot mechanism
Optionally Piloted Vehicle (OPV)	Capable of both manned or unmanned flight operations, typically an adaptation of a general aviation aircraft
Micro Air Vehicle (MAV)	Limited in size to dimension no larger than 15 cm (6 in)
Research UAV	Developed for specific research investigations, typically with no production intent

Low-altitude tactical systems are highly desirable because of their ability to perform dangerous tasks without the risk of losing the pilot. Because the design does not require a pilot, the aircraft can be smaller and more robust than conventional manned platforms with similar performance [15]. Additionally, because of the operating limits imposed on the aircraft by the physical limitations of the human body, pilotless aircraft can have higher performance and larger flight envelopes. Removing the pilot can also result in larger payload capacity or even longer range due to increased fuel capacity. However, the increased capabilities, such as larger flight envelopes, are predicated on adequate aeroelastic performance which may be difficult to achieve.

High-altitude long-duration missions are well-suited to UAVs because of the complex challenges of manning such missions. Special equipment and crew rotations necessary for this mission result in large and heavy aircraft. Again, by eliminating the operators the crafts are much smaller, less-detectable, and able to carry more payload and fuel to perform the same mission as their traditionally manned counterparts [15]. High-altitude missions are also desirable for UAVs from a safety perspective. Few aircraft operate at higher altitudes so issues of traffic management and airspace impingement are reduced. Furthermore, challenges of communication and wind uncertainty are also reduced at higher altitudes. HALE UAVs are also of note for their increased range due to further line-of-sight capability.

Traditionally, robots have been designed to complete "dull, dirty, or dangerous" tasks. In the UAV world—at least thus far—the same holds true. Modern UAVs are designed to collect intelligence, monitor weather, track targets, etc. [14]. The rationale here is that it is less-expensive and less manpower-intensive to operate UAVs in "dull and dirty" situations, and less damaging to a unit to lose a UAV than to lose an aircraft and its pilot in "dangerous" situations. The combination of decreased risk to the pilot and fewer aircraft restrictions leads to the development of faster, lighter, and less-expensive aircraft able to perform traditional manned missions [14]. However, with this comes the fact that smaller militaries and combatants could be able to acquire and develop fleets with similar capabilities to traditionally larger manned fleets. The advantage here lies in the superior UAV

design and performance, part of which includes the aircraft's aeroelastic performance.

The calculation and modeling of aerodynamic vehicle properties is essential to ensure proper flight characteristics. With the proliferation of computers and improvements in processing power, developers are turning more toward computational methods for determining aerodynamic properties [17]. Software based on numerical methods gives designers the ability to reduce the time required to analyze different designs. Similarly, analysis techniques that have not previously been applied to the aeroelastic problem provide new insight and opportunities for more robust designs.

Effective modeling of dynamic systems is one of the most important parts of understanding how they operate. However, dynamic models are often quite complex and difficult to create and implement. Dynamic systems with flexible components further complicate this process and, as with most aircraft, UAVs employ lightweight flexible materials in their construction. While it may be possible to model the UAV as if it were a rigid structure, the real world flexing structure can have drastic effects on the dynamics. This can lead to large discrepancies between the modeled performance and the actual performance. Researchers are thus faced with making very complex models which can take very long and be very expensive. However, by invoking certain assumptions various aspects of the performance can be predicted within an accepted level of accuracy.

1.5. Scope

This thesis aims to apply numerical integration and harmonic balance analysis methods to a typical binary aeroelastic model to gauge their effectiveness and costs. Two models are developed: one with deterministic forcing and one with stochastic forcing. Both models are analyzed via numerical integration while only the deterministic model is also analyzed with a harmonic balance approach. A basic background in aerodynamic and structural analysis is assumed, while relevant sources are included for reference. An applicable structural model is developed in Chapter 2 after which the relevant parameters are defined in the context of a HALE UAV. Chapter 3 provides background information on the aerodynamic model and simplifying assumptions used. Background information on the numerical integration scheme employed for the nonlinear system at hand is given in Chapter 4. The method of harmonic balance is developed in Chapter 5. Chapter 6 presents some stochastic analysis methodology including the basis of the stochastic parameters used. A discussion of the results is included in Chapter 7, and Chapter 8 incorporates some concluding remarks and potential future research areas.

Chapter 2

Structural Model

The model used herein is a simple two-degree-of-freedom (2DOF) airfoil model that accommodates motion in pitch and plunge. The model is referred to in the literature as the typical section and shown in Figure 2-1. The airfoil can pitch about an elastic axis which is defined as being perpendicular to the shear center of the airfoil. The structural stiffness in pitch and plunge is modeled with linear springs. Noteworthy points on the airfoil include the center of gravity, elastic axis, and aerodynamic center. The force model used herein will be discussed in depth in a later chapter.
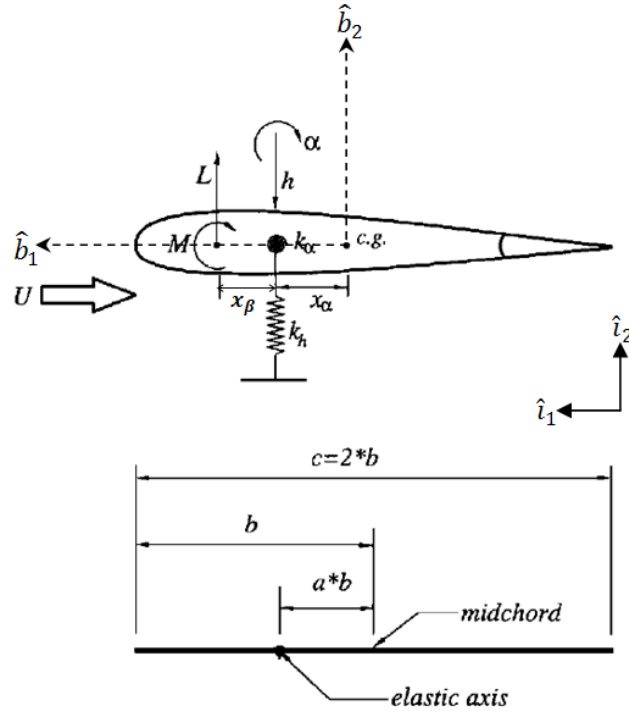
Figure 2-1: Structural Model [18]

2.1. Equations of Motion

Using the above system model from Reference [18] with slight modification, the two-degree-of-freedom equations of motion for pitch (α) and plunge (h) can be derived through the use of Lagrange's Equations by calculating the potential and kinetic energies of the system. The sign convention for both α and h is shown in Figure 2-1 with the arrow pointing in the positive sense. The $\hat{\imath}$ frame is fixed inertially, while the $\hat{b}$ frame is fixed to the airfoil with its origin at the center of gravity and oriented as shown above with the $\hat{b}_1$ axis towards the leading edge. An energy formulation is used to create the equations of motion [2]. The potential

energy consists entirely of the energy stored in the springs and can be modeled with

the equation

$$U = \frac{1}{2}K_h h^2 + \frac{1}{2}K_\alpha \alpha^2 \tag{1}$$

where K_h and K_α are the linear plunging and pitching stiffness coefficients,

respectively.

To calculate the kinetic energy, the velocity of the center of mass—point c.g.

in the figure above—is required.

$$\boldsymbol{V_{CG}} = \boldsymbol{V_{EA}} + \dot{\alpha}\widehat{\boldsymbol{b}}_3 \times x_\alpha \widehat{\boldsymbol{b}}_1 \tag{2}$$

Here, V_{EA} is the velocity of the elastic axis, and x_α is the distance between the

elastic axis and the center of gravity which has been non-dimensionalized by the

semi-chord. The variable x_α is taken to be positive if the center of gravity lies

further towards the trailing edge than the elastic axis does. The symbol $(\,\dot{}\,)$ denotes

the first time derivative whereas the symbol $(\,\ddot{}\,)$ denotes the second time

derivative. Based on the definitions introduced and the coordinate systems chosen,

$$\boldsymbol{V_{EA}} = -\dot{h}\hat{\boldsymbol{i}}_2 \tag{3}$$

and thus

$$\boldsymbol{V_{CG}} = -\dot{h}\hat{\boldsymbol{i}}_2 + \dot{\alpha}x_\alpha\widehat{\boldsymbol{b}}_2 \,. \tag{4}$$

The kinetic energy is then given by

$$T = \frac{1}{2}mV_{CG} \cdot V_{CG} + \frac{1}{2}I_{CG}\dot{a}^2 \tag{5}$$

where I_{CG} is the moment of inertia about the center of mass. Using the relationship

between the inertial and body frames, the kinetic energy can be rewritten as

$$T = \frac{1}{2}m\left(\dot{h}^2 + x_\alpha^2\dot{a}^2\cos(\alpha) + 2x_\alpha\dot{h}\dot{a}\cos(\alpha)\right) + \frac{1}{2}I_{CG}\dot{a}^2 \tag{6}$$

$$T = \frac{1}{2}m\left(\dot{h}^2 + 2x_\alpha\dot{h}\dot{a}\cos(\alpha)\right) + \frac{1}{2}I_{EA}\dot{a}^2, \tag{7}$$

where I_{EA} is the moment of inertia about the elastic axis. It is given by the equation

$$I_{EA} = I_{CG} + mx_\alpha^2\cos^2(\alpha). \tag{8}$$

The next step is to find the generalized forces acting on the system. This is

done by using the method of virtual work where the work done by a virtual

displacement due to the external forces is calculated [2]. The external forces in this

case are the aerodynamic lift and moment. It is assumed that the aerodynamic

forces act at the center of pressure. To calculate the virtual displacement due to the

lift, the velocity of the aerodynamic center is required. That is,

$$V_{AC} = -\dot{h}\hat{i}_2 + \dot{a}x_\beta\hat{b}_2. \tag{9}$$

Then, the virtual displacement due to the lift is

$$\delta P_{AC} = -\delta h\hat{i}_2 + \delta a x_\beta\hat{b}_2. \tag{10}$$

The angular velocity of the wing is $\dot{\alpha}\widehat{\boldsymbol{b}}_3$ which gives the virtual rotation due to the moment as

$$\delta \boldsymbol{R}_{AC} = -\delta\alpha\widehat{\boldsymbol{b}}_3. \tag{11}$$

The total virtual work done by the aerodynamic forces is thus,

$$\overline{\delta W} = L\big[-\delta h + \delta\alpha x_\beta\big] + M\delta\alpha. \tag{12}$$

From this, the generalized forces become

$$\begin{aligned} Q_h &= -L \\ \text{and } Q_\alpha &= M + x_\beta L, \end{aligned} \tag{13}$$

where L and M are the aerodynamic lift force and moment, respectively, and x_β is the distance between the elastic axis and the aerodynamic center. The variable x_β is taken to be positive if the elastic axis lies further towards the trailing edge than the aerodynamic center does. From thin airfoil theory, the aerodynamic center is located at the quarter chord $\left(\frac{c}{4}\right)$ of a symmetric airfoil. Now the equations of motion can be derived by combining all the pieces through the use of Lagrange's Equations as follows [2]. Specifically,

$$\begin{aligned} \frac{d}{dt}\left(\frac{\partial(T-U)}{\partial\dot{h}}\right) - \frac{\partial(T-U)}{\partial h} &= Q_h \\ \text{and } \frac{d}{dt}\left(\frac{\partial(T-U)}{\partial\dot{\alpha}}\right) - \frac{\partial(T-U)}{\partial\alpha} &= Q_\alpha, \end{aligned} \tag{14}$$

Substituting Equations (1), (7), and (13), into Equations (14) the resulting nonlinear undamped, coupled, two degree of freedom aeroelastic equations of motion can be cast in the form

$$m\ddot{h} + mx_\alpha \cos(\alpha)\,\ddot{\alpha} - mx_\alpha \sin(\alpha)\,\dot{\alpha}^2 + K_h h = -L$$

$$I_{EA}\ddot{\alpha} + mx_\alpha \cos(\alpha)\,\ddot{h} + K_\alpha \alpha = M + x_\beta L.$$

(15)

From this system one can see the coupling is the result of the inertial forces and the pitch angle. The offset distance x_α between the center of mass and the elastic axis results in a mass imbalance that causes the bending and torsion modes to become coupled. One can see that if this term were to become zero, as in the case where the center of mass was coincident with the elastic axis, and the pitch displacements were taken to be small such that $\sin(\alpha) \approx 0$ and $\cos(\alpha) \approx 1$, the bending and torsion modes would be completely uncoupled and the inertia and stiffness matrices would be diagonal.

To model the effects of viscous damping, the Rayleigh Dissipation Function is calculated and included in the Lagrange equations. Specifically,

$$D = \frac{1}{2}C_h \dot{h}^2 + \frac{1}{2}C_\alpha \dot{\alpha}^2.$$

(16)

Here, C_h and C_α are the linear plunge and pitch damping coefficients, respectively.

This relationship is incorporated into Lagrange's Equations as

$$\frac{d}{dt}\left(\frac{\partial(T-U)}{\partial \dot{h}}\right) + \frac{\partial D}{\partial \dot{h}} - \frac{\partial(T-U)}{\partial h} = Q_h$$
$$\frac{d}{dt}\left(\frac{\partial(T-U)}{\partial \dot{\alpha}}\right) + \frac{\partial D}{\partial \dot{\alpha}} - \frac{\partial(T-U)}{\partial \alpha} = Q_\alpha.$$

(17)

Substituting Equations (1), (7), (13) and (16), into Equations (17), the nonlinear

damped, coupled, two degree of freedom aeroelastic equations of motion for pitch

and plunge become

$$m\ddot{h} + mx_\alpha \cos(\alpha)\,\ddot{\alpha} - mx_\alpha \sin(\alpha)\,\dot{\alpha}^2 + C_h\dot{h} + K_h h = -\mathrm{L} = L_{tot}$$
$$I_{EA}\ddot{\alpha} + mx_\alpha \cos(\alpha)\,\ddot{h} + C_\alpha\dot{\alpha} + K_\alpha\alpha = M + x_\beta L = M_{tot}.$$

(18)

It is important to note here the assumptions inherent in this model as they

may be the source of future accuracy and/or cost considerations. Specifically, linear

springs have been assumed to model the stiffness in both the pitch and plunge

degrees of freedom. This assumption is warranted because most materials exhibit a

linear elastic region for small deflections. However, if simulations require larger

deflections that exceed this linear region, then the accuracy of the computations will

be reduced. Furthermore, viscous damping has been assumed. This assumes that the

energy dissipated within the system is proportional to the velocity. This is also

assumed to be a linear relationship, which tends to hold fairly accurately for small

deflections but will introduce inaccuracies at larger ones.

2.2. UAV-Specific Parameters

Once the general structural model has been derived, the necessary parameters must be defined. Parameters such as the airfoil dimensions, mass properties, and structural stiffness and damping must be tailored to the particular aircraft and structural model. All of these properties can vary greatly among different aircraft designed for different missions; parameters of HALE UAVs are likely to be much different than those of a supersonic fighter jet. As the aircraft of interest is a HALE UAV, it is useful to examine the properties of existing HALE aircraft.

The first prominent American military HALE UAV was the Predator which was followed by the Reaper and the Global Hawk [19]. Characteristics of these three UAVs are contained within Table 2-1. One can see a large variance in the primary missions and operational capabilities. However, these three UAVs all have similar structural designs to enable high-altitude long-endurance operations as shown in Figure 2-2. By examining the similarities a representative airfoil model can be created for a generic HALE UAV.

Table 2-1: Typical UAV parameters in standard units. Metric units given in parenthesis.

|	**Predator** [20]	**Reaper** [21]	**Global Hawk** [22]
Primary Mission	Armed reconnaissance, airborne surveillance, and target acquisition	Remotely piloted hunter/killer weapon system	High-altitude, long-endurance intelligence, surveillance, and reconnaissance
Thrust	115 hp	900 hp	7600 lbs
Wingspan [ft] (m)	55 (16.75)	66 (20.12)	116 (35.36)
Length [ft] (m)	27 (8.23)	36 (10.97)	44 (13.41)
Height [ft] (m)	6.9 (2.1)	12.5 (3.81)	15.2 (4.63)
Weight/mass [lbs] (kg)	1130 (512.56)	4900 (2222.6)	11,350 (5148.3)
Max Takeoff Weight/mass [lbs] (kg)	2250 (1020.6)	10,500 (4762.7)	26,750 (12,133.6)
Speed [mph] (m/s)	135 (60.35)	230 (102.82)	391 (174.80)
Ceiling [ft] (m)	25,000 (7620)	50,000 (15,240)	60,000 (18,288)
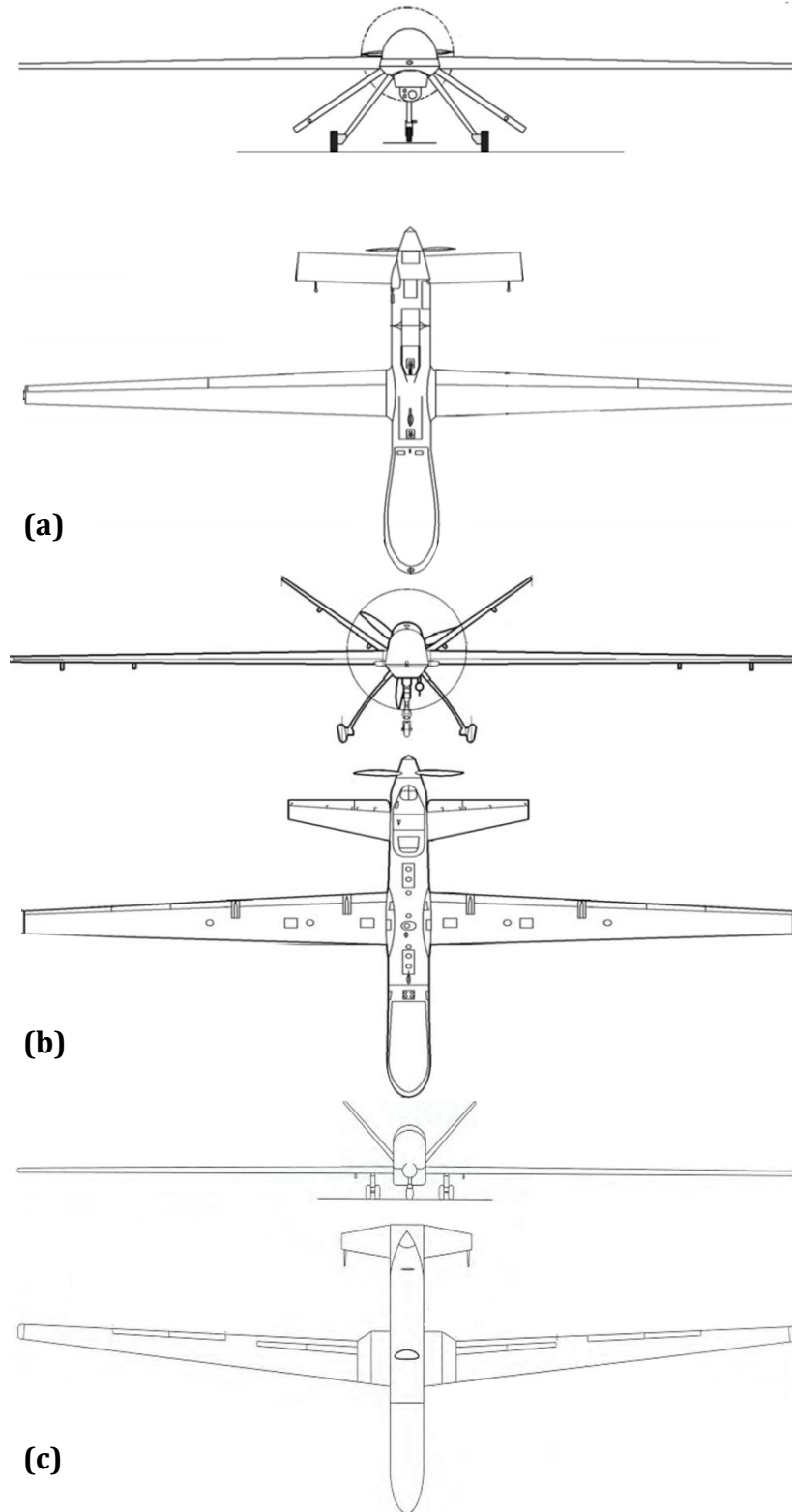
Figure 2-2: Representative HALE UAV Designs. (a) Predator, (b) Reaper, (c) Global Hawk. Note: Not to scale [23]

From Figure 2-2 one can see all three designs contain high aspect ratio wings, the aspect ratio is defined as the ratio of the square of the span to the planform area. Long skinny wings have a high aspect ratio whereas short fat wings have a low aspect ratio. The importance of this design feature is that it reduces the induced drag [5]. This allows the aircraft longer endurance as it requires less fuel to maintain its velocity as a similar aircraft with a lower aspect ratio. One of the drawbacks of high aspect ratio wings is reduced stiffness. Long, lightweight, skinny wings tend to be more flexible than shorter fatter wings. As Reference [13] explains, large span, high aspect ratio wings pose difficulties with respect to aeroelastic phenomena. These difficulties are rooted in the low structural weight fraction necessary for successful HALE designs. Reference [13] continues on to explain the limited understanding of the behavior of HALE designs in the unsteady aerodynamics inherent in aeroelasticity; most work in this area aims to avoid aeroelastic interactions rather than incorporate design features that take advantage of them.

Another similarity among the HALE aircraft designs is the inclusion of cambered wings. Cambered wings produce lift at zero angle of attack. This feature also results in less induced drag than a symmetric wing producing the same amount of lift [5]. The benefit is the same as before: increased endurance. Some other common wing features are sweep, dihedral, and taper. Wing sweep is often used to increase the aircraft's critical Mach number so as to avoid the detrimental effects of supersonic flow and the associated increase in drag when traveling at high subsonic speeds. However, with HALE aircraft, speed is typically not a major design

consideration. Accordingly, the wing sweep used in the three HALE UAVs considered is very small if included at all. Dihedral is mainly used in increasing an aircraft's stability. As dihedral can also increase drag and decrease lift, the HALE designs being considered do not incorporate this feature. Wing taper is often employed to reduce the effects of downwash from tip vortices [5]. Downwash increases induced drag which can decrease endurance. However, in the three designs considered, the taper ratio is very small and as likely the result of weight reduction as the result of induced drag reduction. Taper also contributes to the aspect ratio by reducing the planform area.

Taking into account the various design parameters discussed, a representative model would have a high aspect ratio, a cambered airfoil, and a flexible wing with little to no taper or sweep and no dihedral. Due to the two-dimensional nature of the structural model being studied the flexibility resulting from the high aspect ratio and taper can be evaluated in the stiffness of the springs. Airfoil shape can be chosen so as to incorporate camber. As there is no dihedral and only minimum sweep, the binary nature of the model should capture the full scale dynamics to an acceptable level of accuracy.

The airfoil chosen is the NACA $63_2 - 415$. The NACA 6-series airfoils were developed to maintain laminar flow over a large part of the chord which results in a decreased minimum drag value [24]. The numeric designation of the 6-series contains several important pieces of information about the airfoil. The first number is always 6; this tells the series designation. Chord wise position of maximum

pressure in tenths is represented by the second digit. The third digit denotes the ideal lift coefficient in tenths. Finally, thickness-to-chord ratio is represented by the final two digits. If the designation contains a subscript, it indicates the lift coefficient range in tenths above and below the value of ideal lift coefficient in which favorable pressure gradient and low drag exist [24]. Knowing this information and the shape of the NACA $63_2 - 415$ airfoil depicted in Figure 2-3 one can say it meets the desired camber characteristics with an adequate lift coefficient for a HALE mission. All of the relevant aerodynamic properties necessary for the modeling herein were obtained from the lift and drag curves in Reference [25]. This airfoil has also been used in several published works in various applications and in several production aircraft [26], [27], [28], [29].
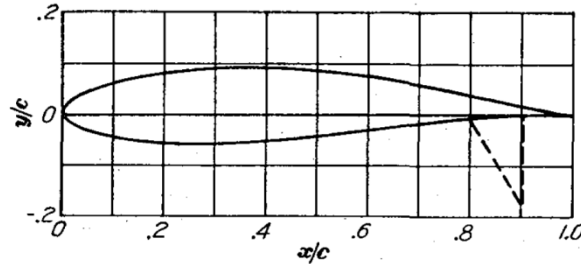
Figure 2-3: NACA $63_2 - 415$ airfoil [25]

Although the bending and torsional stiffness in a three-dimensional wing are dependent on the three-dimensional wing shape and the material of which it is comprised, the model at hand is a rigid two-dimensional airfoil section. Therefore, the bending and torsional stiffness represented by the linear springs in Equations (18) should be chosen to be representative of the three-dimensional wing bending and torsional stiffness. One way to do this is by applying the assumed modes

method [30]. The assumed modes method extends the principle of virtual

displacements to produce a generalized parameter model of a continuous system

that approximates the flexible behavior of the system [30]. Also referred to as the

Ritz method, the advantage is the ability to reduce an infinite degree of freedom

problem to one with n manageable degrees of freedom while maintaining

reasonable accuracy. The n degrees of freedom result from the n assumed modes. By

increasing the number of assumed modes, the reduced order approximation

converges to the original infinite degree of freedom system [2]. Following the

derivations in either Reference [2], [30], [31], or [32], if the wing is approximated as

a beam, the potential bending strain energy can be calculated as follows:

$$U = \frac{1}{2} \int_0^s EI \left(\frac{\partial^2 z}{\partial y^2} \right)^2 dy \tag{19}$$

Here, z is taken to be the transverse deflection based on an assumed bending shape,

y is the span-wise coordinate along the wing, s is the wing span, and EI is the

flexural rigidity. The bending deformation can be described by the expression

$$z(y, t) = \psi(y)q(t) = \left(\frac{y}{s} \right)^2 q(t) \tag{20}$$

containing an assumed deformation shape, ψ. Here q is taken to be the coordinate of

interest, and s is the span of the finite wing. Note the chosen quadratic assumed

shape. Substituting Equation (20) into Equation (19) and solving yields the potential

bending strain energy of the finite wing. That is,

$$U = \frac{1}{2} \int_0^s EI \left(\frac{2}{s^2} q \right)^2 dy = \frac{2EI}{s^3} q^2. \tag{21}$$

As done before in Equation (1), the potential energy of a spring is found using the

equation

$$U = \frac{1}{2} K_h q^2. \tag{22}$$

Combining Equation (21) and Equation (22), the expression for the equivalent

bending stiffness

$$K_h = \frac{4EI}{s^3} \tag{23}$$

can be expressed in terms of the flexural rigidity.

An analogous method can be applied to the torsional component resulting in

the following expression for the equivalent torsional stiffness in terms of the

torsional rigidity, *GJ.* Here a linear displacement shape is assumed yielding

$$K_\alpha = \frac{GJ}{s}. \tag{24}$$

The only other remaming step for obtaining K_α and K_h involves choosing

torsional and flexural rigidity values representative of a HALE UAV. While this

method is not exact, it is a very good engineering approximation to capture the finite

wing structural parameters with only a 2DOF airfoil model. Increasing the number

of assumed mode shapes will result in a better approximation. To base the selection

of the flexural and torsional rigidities on common engineering practice, the values

used in the Goland wing model of Reference [33] are used. However, the Goland

wing has an aspect ratio less than 5. In order to match the HALE UAV aspect ratios of

approximately 15-20, the span used in equating the finite wing stiffness to the

equivalent spring stiffness in Equations (23) and (24) is scaled up. The effect of this

scaling is to sufficiently model the stiffness of the high aspect ratio wing as modeled

by the chosen 2DOF model. The final flexural and torsional rigidity values are

provided in Table 2-2 below.

In the final model the chord length is chosen based on the three HALE UAVs

studied earlier. Reference [23] gives the root chord dimensions as being between

roughly 3.5 ft and 6 ft. The value of 6 feet is chosen to be representative of the three

HALE UAVs and also applicable to the Goland wing structural values. Wing density is

taken from the Goland model. The remaining parameters are calculated based on

the chord length, span length, density, and flexural and torsional rigidity vales. Small

viscous damping terms are included based on the assertions made in Reference [3].

The damping is taken to be proportional to the stiffness. The resulting values for the

various design parameters are given in Table 2-2.

Table 2-2: Structural Model Parameters

Mass	m	$35.72\ kg$
Moment of Inertia about Elastic Axis	I_{EA}	$8.60\ kg\ m^2$
Chord length	c	$1.83\ m$
Finite wing span length	s	$30.48\ m$
2DOF airfoil span length	l	$1\ m$
Distance between elastic axis and center of gravity non-dimensionalized by the semi-chord	x_α	0.2
Distance between the elastic axis and the aerodynamic center	x_β	$0.1463\ m$
Flexural rigidity	EI	$9.75*10^6\ N\ m^2$
Torsional rigidity	GJ	$9.83*10^5\ N\ m^2$
Linear plunge stiffness coefficient	K_h	$1.38*10^3\ N/m$
Linear pitch stiffness coefficient	K_α	$3.23*10^4\ \dfrac{Nm}{rad}$
Proportional damping value	ε	10^{-3}
Linear plunge damping coefficient	C_h	$\varepsilon K_h\ \dfrac{N}{m}$
Linear pitch damping coefficient	C_α	$\varepsilon K_\alpha\ \dfrac{Nm}{rad}$

In the simulations, the aircraft is assumed to be traveling at 30,000 ft altitude which is representative of HALE UAV operations as shown in Table 2-1. The airfoil model is given a prescribed initial deflection in both the pitch and plunge degrees of freedom of $h(0) = h_0 = -0.1\,m,\ \alpha(0) = \alpha_0 = 6°$. The initial pitch and plunge rates are taken to be zero. These initial conditions represent the aircraft flying at a small angle of attack and experiencing small static wing bending under the applied lift force or perhaps the initial deflections produced by a disturbance such as a wind gust. A similar scenario would be seen in a real world flight of a similar aircraft with flexible wings. Additional model details specific to the various analysis methods will be included in their respective ensuing chapters.

Chapter 3

Aerodynamic Modeling

In order to accurately model the forces experienced by an airfoil, one must understand the basics of aerodynamic theory. The continuity equation and Bernoulli's equation provide a basis for understanding the generation of aerodynamic lift. As airflow encounters an airfoil it splits into two different flows: one above the airfoil and one below it. With a cambered airfoil or a symmetric airfoil at an angle of attack, the flow over the top of the airfoil is constricted more than the flow underneath the airfoil. This causes the flow over the top to increase in velocity to satisfy the continuity equation. Any increase in the fluid velocity must also be met with a decrease in the fluid pressure to satisfy Bernoulli's equation. Lift results from the difference in the low pressure above the airfoil and the higher pressure below the airfoil [5].

From aerodynamic theory one knows that the lift force, L, exerted on an airfoil by the airflow around it is given by the equation

$$L = \tfrac{1}{2}\rho V^2 C_{L_\alpha}\alpha S, \tag{25}$$

where ρ is the air density, V is the free stream air velocity, C_{L_α} is the lift curve slope, α is the angle of attack, and S is a characteristic area. The resulting force acts at the center of pressure. The expression of the aerodynamic moment is similar but includes a necessary moment arm

$$M = \tfrac{1}{2}\rho V^2 C_M S c, \tag{27}$$

where C_M is the moment coefficient and c is the chord length. The resulting moment is centered at the aerodynamic center of the airfoil and remains relatively constant for varying angles of attack [34]. According to thin airfoil theory, the aerodynamic center is located at the quarter-chord for symmetric airfoils [35]. As Figure 2-3 shows, the chosen airfoil is not symmetric. However, even with cambered airfoils, the aerodynamic center is close to the quarter-chord for subsonic speeds [34]. The expressions in Equations (25) and (27) are valid for steady airflow where the density and velocity are constant and the airfoil is steady.

Another important aspect of aerodynamic modeling is compressibility. The expressions in Equations (25) and (27) assume incompressible flow. This assumption is warranted for free stream velocities under approximately 100 m/s. When the free stream velocity exceeds this speed the large pressure changes

experienced by the airflow can result in large density changes. Density fluctuations affect the magnitudes of the lift and drag produced by the airflow over the airfoil [5]. To account for compressibility effects the Prandtl-Glauert correction is used. This correction is based on the linearized velocity potential equation and is applicable for Mach numbers approximately between 0.3 and 0.7. Mach numbers higher than 0.7 produce transonic effects which must be addressed through other means. Compressibility is neglected for flows below Mach 0.3.

The interdependency of the airfoil motion and aerodynamic forces poses a challenge to aeroelasticians. Most classical aerodynamic theory is based on steady flow or steady motion, but aeroelastic problems often involve time-dependent fluid motion [6]. Airfoils undergoing aeroelastic interactions oscillate in the flow which alters the circulation about the airfoil. The study of this time-dependent fluid motion is called unsteady aerodynamics. Aerodynamic forces acting on a body oscillating in an unsteady flow are generated by vorticity (or circulation) and apparent mass (or inertial) contributions [3]. These two categories are referred to as circulatory and non-circulatory, respectively. Due to the Helmholtz theorem, the total circulation must be zero. When the circulation about the airfoil changes vortices are shed into the wake to balance the overall circulation [2]. Shed vortices affect the flow field by imparting unsteady flow back to the airfoil. This influence decreases as the vortex travels away from the airfoil. Based on this complex interaction, completely modeling unsteady aerodynamics is very involved and not well-understood. Theodorsen [36] and Wagner [37] have both put forth unsteady aerodynamic models, and complex computational fluid dynamics (CFD) software can model these

effects, but all of them must be formulated in such a way as to interface with the necessary structural model. The computational resources required for these models are also very costly.

As stated in Reference [38], a complete understanding of unsteady airfoil behavior has not been attained. However, by studying experimental data some qualitative models have been produced which encompass the essential physics involved [38]. One of the biggest challenges of unsteady aerodynamic modeling is dynamic stall. An oscillating airfoil may experience large angle of attack variations which result in flow separation, stall, and reattachment. This sequence generates large variations in the lift as compared to those predicted by simpler quasi-steady models. However, the quasi-steady models can still produce insightful results [38].

The quasi-steady assumption states that the aerodynamic characteristics of a moving airfoil can be equated to the aerodynamic characteristics of the same airfoil when sampled instantaneously at discrete points in time [3]. In other words, the aerodynamic characteristics of a moving airfoil are taken to be a function of only the instantaneous properties of the airfoil. Rather than the current aerodynamic forces being influenced by shed vortices and other unsteady effects, the instantaneous lift and moment are calculated using only the instantaneous angle of attack, free stream velocity, and pitch and plunge rates. It follows that when calculating the forces using such a model, increasingly smaller time steps will better approximate the forcing of the complete system. Even so, it is important to note that the unsteady effects may

have important influence on the results. Equations for calculating the quasi-steady lift and moment coefficients are as [3]:

$$C_{L_{qs}} = C_{L_\alpha}\left[\alpha + \frac{\dot{h}}{V} + b\left(\frac{1}{2} - a\right)\frac{\dot{\alpha}}{V}\right]$$

$$\text{and } C_{M_{qs}} = -\frac{c\pi}{8V}\dot{\alpha},$$

(28)

where b is the semi-chord and a is a nondimensional parameter denoting the location of the elastic axis as shown in Figure 2-1. These equations take into account motion of the airfoil through the pitch and plunge rates. The advantage of the quasi-steady assumption over full unsteady aerodynamics is that computational requirements are reduced while still achieving reasonably accurate qualitative behavior. Further, depending on how the model is set up, the effects of structural nonlinearities can be distinguished from those of the unsteady aerodynamics. As mentioned above, both circulatory and non-circulatory forces are encountered in aeroelasticity. However, as Reference [3] points out, the non-circulatory terms are neglected in the quasi-steady assumption as their contributions to the simple bending-torsion airfoil flutter of a cantilever wing are negligible. For the purposes of gaining initial insight into the aeroelastic problem the quasi-steady assumption is used in the aerodynamic modeling of this paper.

Using the quasi-steady assumption along with the linear lift curve slope are likely sources of error. For the airfoil used, the linear region of the lift curve slope is valid for angles of attack between approximately ±12° as shown in Figure 3-1. As

dynamic stall behavior has not been included in this model, angles of attack larger
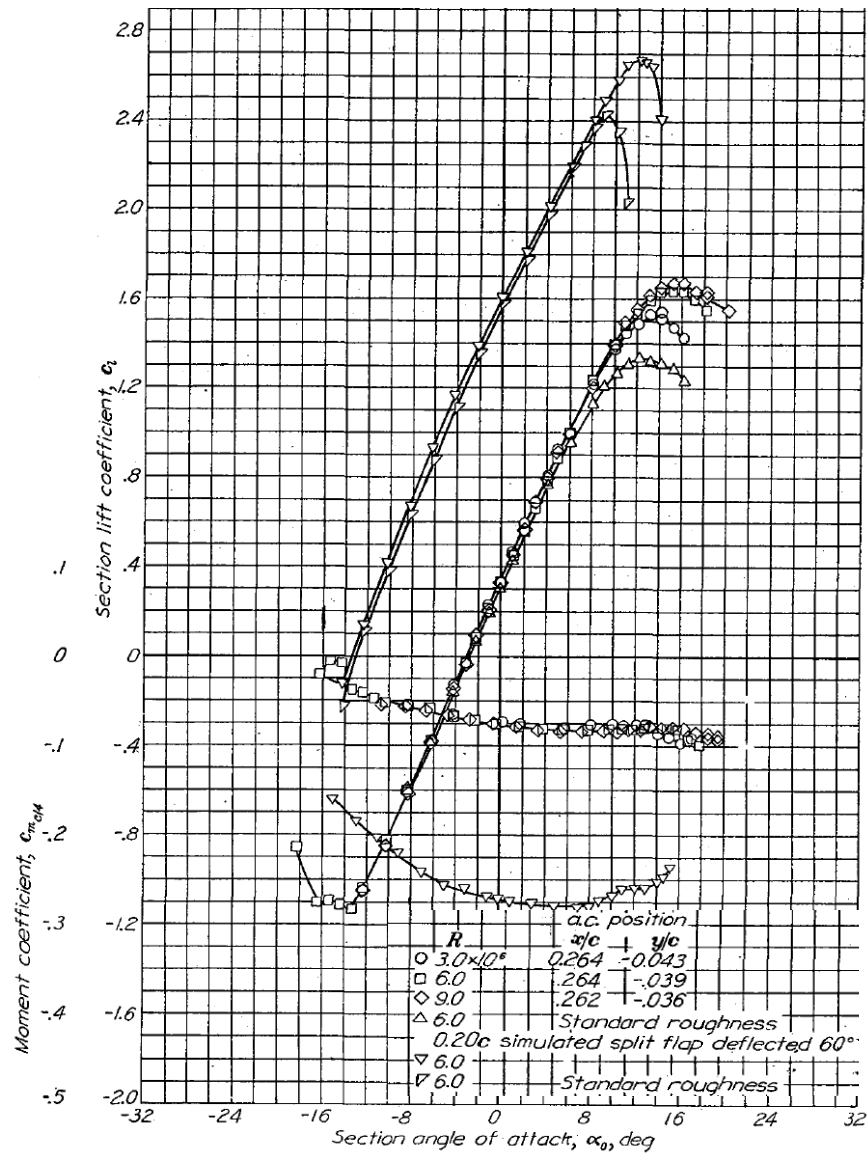
than ±12° are likely to give results that are incorrect.

Figure 3-1: Lift Curve for the NACA $63_2 - 415$ Airfoil [25]

Chapter 4

Numerical Integration

Once the nonlinear equations of motion have been determined and an

applicable aerodynamic model has been chosen, the next step is to adopt an

appropriate method of analysis. The complex nature of nonlinear equations has

resulted in many different analytical techniques including numerical integration,

equivalent linearization, perturbation methods, and harmonic balance [39]. One of

the methods chosen for comparison herein is direct numerical integration. Several

algorithms exist which provide this capability, although as with other methods,

there are advantages and disadvantages. The advantages include limited initial

effort and some algorithms display unconditional stability. Most algorithms require

only the equations of motion, initial conditions, time step, and desired tolerance.

One of the biggest drawbacks is cost; most numerical integration algorithms require

very small step sizes for precise convergence which results in lengthy computation

time. If the goal of solving the equations is to determine the steady state response, this may result in quite lengthy time spans that, when combined with very small step sizes, can be computationally prohibitive. However, with the use of today's computing power most simple equations can be numerically integrated to reasonable accuracy within an acceptable amount of time.

4.1. Application

The numerical integration scheme used herein is contained within the Matlab command ODE45. This algorithm is based on the explicit Runge-Kutta (4, 5) formula defined by the Dormand-Prince pair [40]. This pair is a 4th and 5th order approximation which has the benefits of extended regions of absolute stability and small principle truncation terms. ODE45 is a one-step solver in that it requires only the solution of the previous time step to compute the solution at the subsequent time step. This numerical integration scheme is chosen for its accurate results and simple implementation. Implementation of this scheme requires that the 2nd order nonlinear equations given by Equations (18) be recast as a 1st order system

$$\frac{dy_1}{dt} = y_3,$$

$$\frac{dy_2}{dt} = y_4,$$

$$\frac{dy_3}{dt} = -x_\alpha \cos(y_2)\frac{dy_4}{dt} + x_\alpha y_4^2 \sin(y_2) - \frac{C_h}{m}y_3 - \frac{K_h}{m}y_1 - \frac{L}{m}, \tag{29}$$

$$\text{and } \frac{dy_4}{dt} = -\frac{mx_\alpha \cos(y_2)}{I_{EA}}\frac{dy_3}{dt} - \frac{C_\alpha}{I_{EA}}y_4 - \frac{K_\alpha}{I_{EA}}y_2 + \frac{M}{I_{EA}} + \frac{x_\beta L}{I_{EA}},$$

where $y_1 = h, y_2 = \alpha, y_3 = \dot{h}$, and $y_4 = \dot{\alpha}$.

The ODE45 command also requires initial conditions as well as the desired

error tolerances and time span of integration. The error tolerances specify the

desired accuracy of each iteration in order to reduce any error propagation within

the calculations. The time step need not be specified as the algorithm chooses its

own step size at each iteration to achieve the desired accuracy [41]. However, to

increase accuracy—at the cost of computation time—one can specify an initial time

step as well as a maximum time step. The values used in the computations herein

are given in Table 4-1 below along with the initial conditions presented earlier in

section 2.2.

Table 4-1: Numerical Integration Parameters

Absolute Tolerance	abstol	10^{-6}
Relative Tolerance	reltol	10^{-5}
Initial Step Size	InitialStep	10^{-4}
Maximum Step Size	MaxStep	10^{-3}

As a basis for the accuracy of the numerical integration method used—and

due to the lack of experimental data for the nonlinear system model being

analyzed—a generic linear problem is solved both numerically and analytically. The

example system had the following form:

$$M\ddot{x} + C\dot{x} + Kx = F, \tag{30}$$

where M, C, and K are 2x2 mass, damping, and stiffness matrices, respectively; x is a

2x1 state vector; and $\boldsymbol{F}$ is a 2x1 forcing vector. The values and theory used in this

problem are from Reference [42]. The pertinent numerical values are

$$\boldsymbol{M} = \begin{bmatrix} 1 & 0 \\ 0 & 2 \end{bmatrix}, \boldsymbol{C} = \begin{bmatrix} 0.3 & -0.2 \\ -0.2 & 0.3 \end{bmatrix}, \boldsymbol{K} = \begin{bmatrix} 10 & -6 \\ -6 & 22 \end{bmatrix}, \boldsymbol{x} = \begin{bmatrix} x_1 \\ x_2 \end{bmatrix}, \boldsymbol{F} = \begin{bmatrix} \cos{(3t)} \\ -\cos{(3t)} \end{bmatrix}. \tag{31}$$

As shown in Figure 4-1, the system was numerically integrated and compared to the

exact analytical steady-state solution from classical vibration theory. The error

between the two methods using the numerical algorithm described above with the

parameters in Table 4-1 is negligible. Based on this data one can reasonably say the

numerical integration procedure gives accurate results.

Once the numerical integration scheme is validated, it is coupled with the

quasi-steady aerodynamic model. As shown in Figure 4-2, the process is rather

simple. The initial set up for this algorithm is quite straight forward and consists of

casting the equations of motion in the form given in Equation (29) and defining all

the relevant parameters for the simulation (mass, chord, stiffness, time step, etc.).
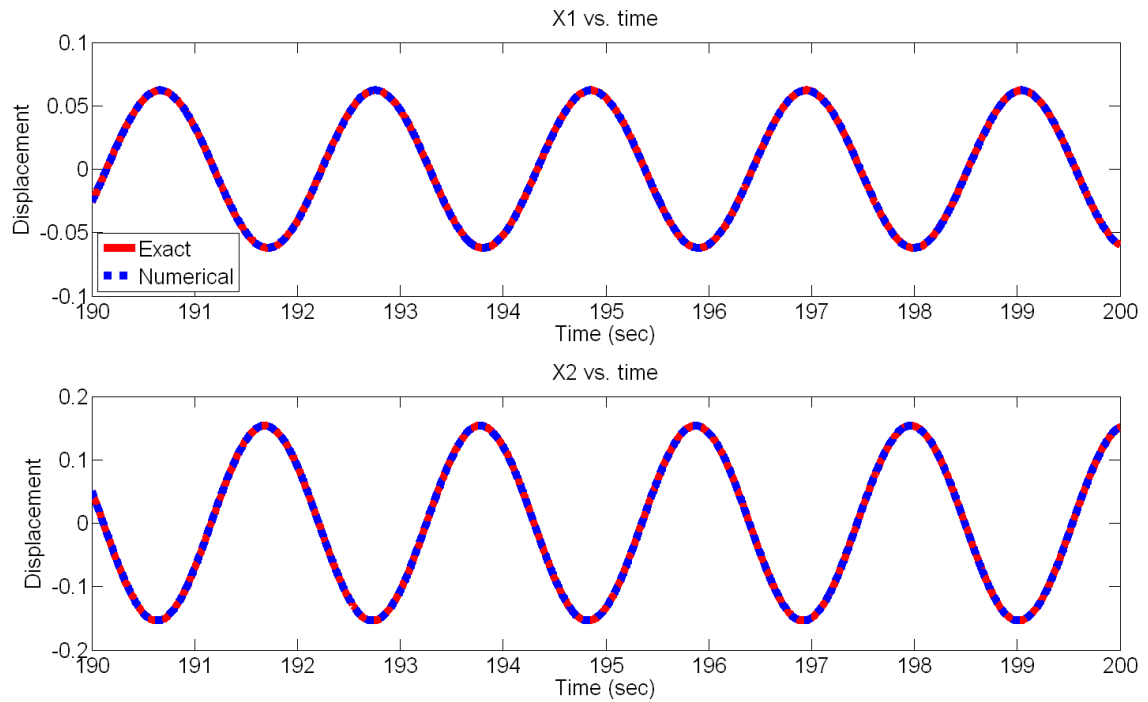
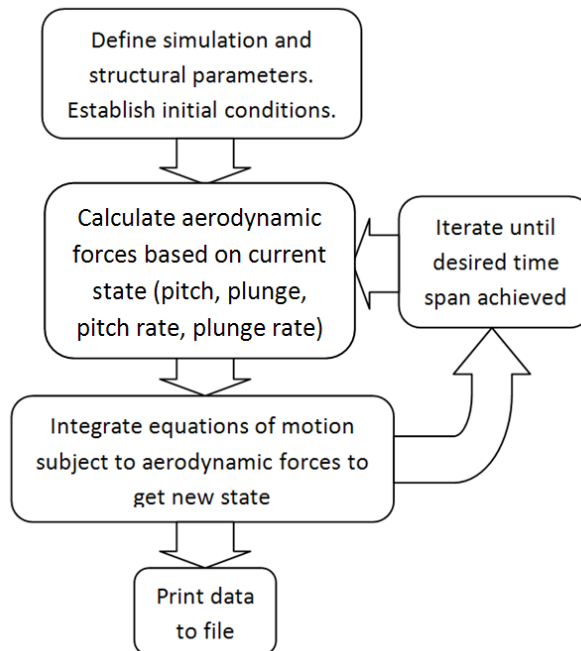**Figure 4-1: Comparison of Numerical Results with Exact Steady-State Solution**

Figure 4-2: Coupled Aerodynamic Model and Numerical Integration Algorithm

Chapter 5

Harmonic Balance

Another nonlinear analytical method applied to the problem at hand is harmonic balance. Herein, harmonic balance is chosen as one way to predict the steady-state behavior of the system subjected to harmonic forcing. This method, though limited to cases of harmonic excitation, is deemed applicable to aeroelastic analysis as the lift and moment forces present during aeroelastic interactions can often excite steady state oscillatory responses (LCO) in both pitch and plunge. LCO are more common in transonic flight conditions than subsonic conditions. For this reason, some researchers have attributed LCO mostly to the nonlinear aerodynamic forcing [43]. However, the understanding of nonlinear systems and LCO—especially in the context of aeroelasticity—is incomplete and thus no definitive correlations can be made. Reference [43] examines the effects of nonlinear transonic

aerodynamics on the production of LCO using a harmonic balance approach building on Reference [44].

The method of harmonic balancing is employed through the use of a Fourier series expansion. The forcing terms are modeled as an nth-order Fourier series expansion of which all the necessary coefficients can be computed from the known forcing function. The steady-state response of the system is also assumed to be an nth-order Fourier series expansion. The excitation and the assumed response are then substituted into the equations of motion and harmonic terms of the same frequency are grouped together. This results in a system of *2n* linear equations for each degree of freedom which are solved for the *2n* unknown coefficients of the assumed Fourier series expansion of the steady-state response [45]. Often it is found that only a single fundamental frequency is required for accurate results, although additional higher-order components can be added for better accuracy at the cost of increased computation time [39]. The author of Reference [45] has found this method applicable even for problems in which the nonlinear terms are large.

5.1. Application

To apply the method to the problem at hand, the lift and moment terms are assumed to be nth-order purely harmonic terms of the form:

$$
\begin{aligned}
L_{tot} &= L_1 \sin(\tau) + L_2 cos(\tau) + \cdots + L_{2n-1} \sin(n\tau) + L_{2n} \cos(n\tau), \\
\text{and } M_{tot} &= M_1 \sin(\tau) + M_2 cos(\tau) + \cdots + M_{2n-1} \sin(n\tau) + M_{2n} \cos(n\tau)
\end{aligned}
\tag{32}
$$

where $\tau = \omega t$. Note here that the Fourier series expansions are taken to have zero-mean. This has been done to reflect the zero-mean behavior of the response of the actual system. The plunge and pitch responses are also assumed to be zero-mean nth-order harmonic terms of the form

$$
\begin{aligned}
h &= h_1 \sin(\tau) + h_2 \cos(\tau) + \cdots + h_{2n-1} \sin(n\tau) + h_{2n} \cos(n\tau), \\
\text{and } \alpha &= \alpha_1 \sin(\tau) + \alpha_2 \cos(\tau) + \cdots + \alpha_{2n-1} \sin(n\tau) + \alpha_{2n} \cos(n\tau)
\end{aligned}
\tag{33}
$$

If n is taken to equal 1, Equations (32) and (33) reduce to

$$
\begin{aligned}
L_{tot} &= L_1 \sin(\tau) + L_2 \cos(\tau), \\
M_{tot} &= M_1 \sin(\tau) + M_2 \cos(\tau), \\
h &= h_1 \sin(\tau) + h_2 \cos(\tau), \\
\text{and } \alpha &= \alpha_1 \sin(\tau) + \alpha_2 \cos(\tau).
\end{aligned}
\tag{34}
$$

Plugging Equations (34) into Equations (18) yields

$$
\begin{aligned}
-m\omega^2 h_1 &\sin(\tau) - m\omega^2 h_2 \cos(\tau) - mx_\alpha \omega^2 \alpha_1 \cos\big(\alpha_1 \sin(\tau) + \alpha_2 \cos(\tau)\big) \sin(\tau) \\
&- mx_\alpha \omega^2 \alpha_2 \cos\big(\alpha_1 \sin(\tau) + \alpha_2 \cos(\tau)\big) \cos(\tau) \\
&- mx_\alpha \omega^2 \alpha_1^2 \sin\big(\alpha_1 \sin(\tau) + \alpha_2 \cos(\tau)\big) \cos^2(\tau) \\
&- mx_\alpha \omega^2 \alpha_2^2 \sin\big(\alpha_1 \sin(\tau) + \alpha_2 \cos(\tau)\big) \sin^2(\tau) \\
&+ mx_\alpha \omega^2 \alpha_1 \alpha_2 \sin\big(\alpha_1 \sin(\tau) + \alpha_2 \cos(\tau)\big) \sin(\tau) \cos(\tau) \\
&+ C_h \omega h_1 \cos(\tau) - C_h \omega h_2 \sin(\tau) + K_h h_1 \sin(\tau) + K_h h_2 \cos(\tau) \\
&= -L_1 \sin(\tau) - L_2 \cos(\tau)
\end{aligned}
\tag{35}
$$

$$
\tag{36}
$$

and

$$-I_{EA}\omega^2\alpha_1\sin(\tau) - I_{EA}\omega^2\alpha_2\cos(\tau)$$
$$- mx_\alpha\omega^2 h_1\cos(\alpha_1\sin(\tau) + \alpha_2 cos(\tau))\sin(\tau)$$
$$- mx_\alpha\,\omega^2 h_2\cos(\alpha_1\sin(\tau) + \alpha_2 cos(\tau))\cos(\tau) + C_\alpha\omega\alpha_1\cos(\tau)$$
$$- C_\alpha\omega\alpha_2\sin(\tau) + K_\alpha\alpha_1\sin(\tau) + K_\alpha\alpha_2 cos(\tau)$$
$$= M_1\sin(\tau) + M_2 cos(\tau).$$

The complex nonlinear nature of these equations makes generating and solving the system of *2n* linear equations for the unknown coefficients computationally prohibitive. To solve this problem, the original equations of motion—Equations (18)—are linearized and analyzed with the harmonic balance method to derive an initial estimate of the coefficients of the nonlinear problem. To solve the nonlinear equations—Equations (35) and (36) —orthogonality is enforced and the equations are averaged over an interval as in Reference [46] resulting in *2n* equations for each degree of freedom. Specifically,

$$-\frac{1}{2}m\omega^2 h_1 - \frac{1}{2}C_h\omega h_2 + \frac{1}{2}K_h h_1$$

$$+ \omega^2 m x_\alpha \left[-\alpha_1 \int_0^{\frac{2\pi}{\omega}} \cos(\alpha_1 \sin(\tau) + \alpha_2 \cos(\tau)) \sin^2(\tau) \, dt \right.$$

$$- \alpha_2 \int_0^{\frac{2\pi}{\omega}} \cos(\alpha_1 \sin(\tau) + \alpha_2 \cos(\tau)) \sin(\tau) \cos(\tau) \, dt$$

$$- \alpha_1^2 \int_0^{\frac{2\pi}{\omega}} \sin(\alpha_1 \sin(\tau) + \alpha_2 \cos(\tau)) \cos^2(\tau) \sin(\tau) \, dt \tag{37}$$

$$- \alpha_2^2 \int_0^{\frac{2\pi}{\omega}} \sin(\alpha_1 \sin(\tau) + \alpha_2 \cos(\tau)) \sin^3(\tau) \, dt$$

$$\left. + \alpha_1 \alpha_2 \int_0^{\frac{2\pi}{\omega}} \sin(\alpha_1 \sin(\tau) + \alpha_2 \cos(\tau)) \cos(\tau) \sin^2(\tau) \, dt \right] = -\frac{1}{2}L_1$$

$$-\frac{1}{2}m\omega^2 h_2 + \frac{1}{2}C_h\omega h_1 + \frac{1}{2}K_h h_2$$

$$+ \omega^2 m x_\alpha \left[-\alpha_1 \int_0^{\frac{2\pi}{\omega}} \cos(\alpha_1 \sin(\tau) + \alpha_2 \cos(\tau)) \sin(\tau) \cos(\tau) \, dt \right.$$

$$- \alpha_2 \int_0^{\frac{2\pi}{\omega}} \cos(\alpha_1 \sin(\tau) + \alpha_2 \cos(\tau)) \cos^2(\tau) \, dt$$

$$- \alpha_1^2 \int_0^{\frac{2\pi}{\omega}} \sin(\alpha_1 \sin(\tau) + \alpha_2 \cos(\tau)) \cos^3(\tau) \, dt \tag{38}$$

$$- \alpha_2^2 \int_0^{\frac{2\pi}{\omega}} \sin(\alpha_1 \sin(\tau) + \alpha_2 \cos(\tau)) \sin^2(\tau) \cos(\tau) \, dt$$

$$\left. + \alpha_1 \alpha_2 \int_0^{\frac{2\pi}{\omega}} \sin(\alpha_1 \sin(\tau) + \alpha_2 \cos(\tau)) \sin(\tau) \cos^2(\tau) \, dt \right] = -\frac{1}{2}L_2$$

$$-\frac{1}{2}I_{EA}\omega^2 \alpha_1 - \omega^2 h_1 m x_\alpha \int_0^{\frac{2\pi}{\omega}} \cos(\alpha_1 \sin(\tau) + \alpha_2 \cos(\tau)) \sin^2(\tau) \, dt$$

$$- \omega^2 h_2 m x_\alpha \int_0^{\frac{2\pi}{\omega}} \cos(\alpha_1 \sin(\tau) + \alpha_2 \cos(\tau)) \cos(\tau) \sin(\tau) \, dt \tag{39}$$

$$- \frac{1}{2}C_\alpha \omega \alpha_2 + \frac{1}{2}K_\alpha \alpha_1 = \frac{1}{2}M_1$$

$$-\frac{1}{2}I_{EA}\omega^2\alpha_2 - \omega^2 h_1 mx_\alpha \int_0^{\frac{2\pi}{\omega}} \cos(\alpha_1 \sin(\tau) + \alpha_2 \cos(\tau)) \cos(\tau) \sin(\tau)\, dt$$

$$- \omega^2 h_2 mx_\alpha \int_0^{\frac{2\pi}{\omega}} \cos(\alpha_1 \sin(\tau) + \alpha_2 \cos(\tau)) \cos^2(\tau)\, dt + \frac{1}{2}C_\alpha \omega \alpha_1 \qquad (40)$$

$$+ \frac{1}{2}K_\alpha \alpha_2 = \frac{1}{2}M_2.$$

The resulting expressions—Equations (37)-(40)—contain nonlinear integral terms. Using α_1 and α_2 from the linear approximation as an initial estimate, the nonlinear integrals are determined numerically and the result is then substituted back into Equations (37)-(40) resulting in a system of $2n$ linear equations of the unknown coefficients for each degree of freedom. The system is solved for new values of the coefficients which are used to re-evaluate the nonlinear integrals and generate new values of the unknown coefficients. This iterative process is continued and coefficient values at each iteration are compared to the values at the previous iteration. Once a specified tolerance between successive iterations is reached, the final coefficients are then taken to be the correct ones as assumed in Equations (34). A flow chart describing the computational process is included blow in Figure 5-1.

In mechanizing this method, the initial set up is rather involved. The equations—Equations (37)-(40)—must be derived in addition to the linear harmonic balance equations. The complexity of these equations is dependent on the order of the Fourier series used. Once the method is implemented, however, the computations only require several seconds to run depending on the tolerance used. Using a tolerance of 10^{-4} requires only 2-3 iterations and less than five seconds.

Figure 5-1 details the process of the harmonic balance solver. Once the coefficients

are solved for using this algorithm the assumed responses given in Equations (34)

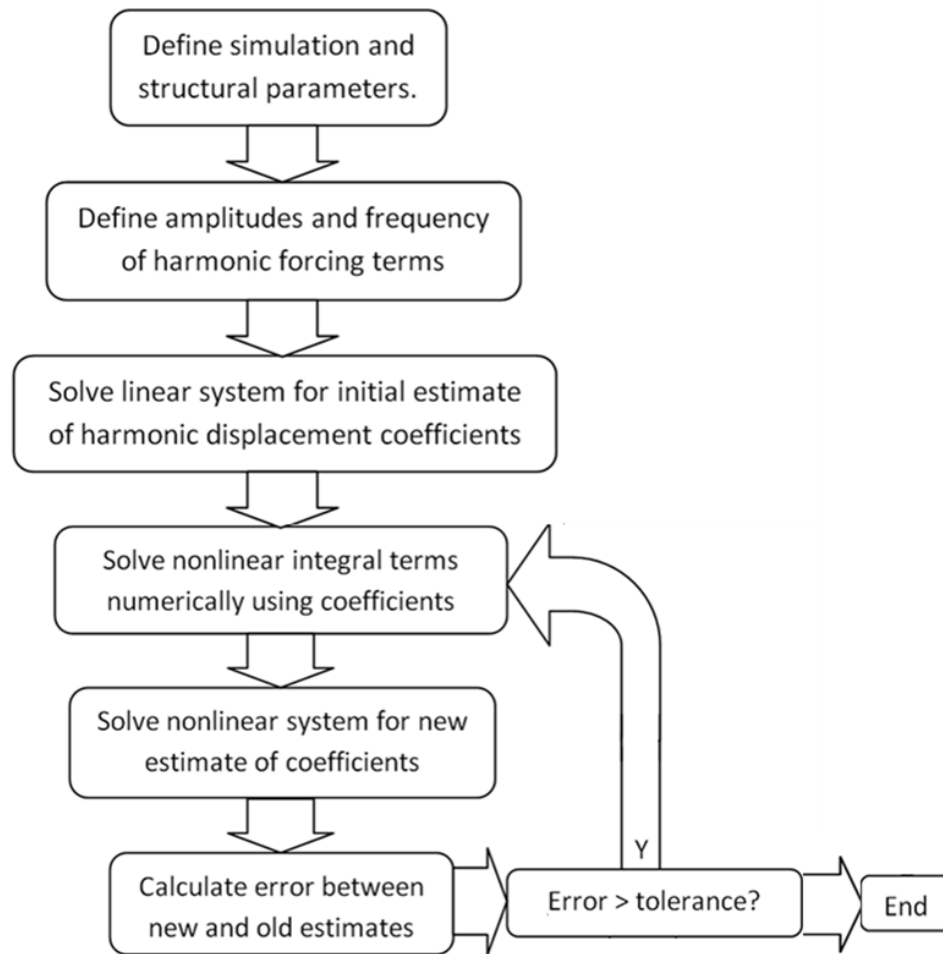can be plotted and compared against the time integration results.

Figure 5-1: Harmonic Balance Solver Algorithm

Chapter 6

Stochastic Modeling

Once the structural equations of motion, aerodynamic modeling, and time integration pieces have been completed, another relevant behavior to investigate is that due to stochastic excitation. The use of stochastic excitation within the construct of aeroelasticity is of use based on the source of the excitations. Aerodynamic lift and moment forces are generated through the interaction of airflow over an airfoil. Often, the airflow is laminar and smooth resulting in a constant force. However, anyone who has ridden in an airplane knows that aircraft often experience turbulence. Turbulence can cause a number of changes within the production of aerodynamic forces. Varying air velocities can cause the resulting force to vary as the relationship between the force and the air velocity is of the order of velocity squared (see Equation (25)). Further, turbulent airflow over an airfoil can result in separation which reduces the magnitude of lift and moment

while producing additional drag. These issues are apparent for any airfoil traveling

through the atmosphere, but become especially important to consider for airfoils

experiencing aeroelastic interactions which can result in motion of the airfoil as well

as phenomena such as vortex shedding and stall. The model herein does not

explicitly account for separation effects, but does account for changes in lift and

moment based on a stochastic velocity input.

6.1. Turbulence Modeling

Wind turbulence has been studied for many decades. Interactions between

wind and structures are important to understand as history has shown through

catastrophes like the Tacoma-Narrows bridge collapse. Over the years researchers

have developed models of wind turbulence based on theory and empirical data. One

of the most widely used models is the von Karman spectrum attributed to its

developer, Theodore von Karman. It was later adapted for use in wind engineering

[47]. The von Karman spectrum represents the gust velocity power spectral density

and has different forms for the vertical/lateral components and the longitudinal

component. Herein the longitudinal component of the gust is considered. The

pertinent expression is

$$S_u(\omega) = \frac{2\sigma_u{}^2 L_u}{\pi V} \frac{1}{\left[1 + \left(1.339 L_u \frac{\omega}{V}\right)^2\right]^{5/6}}, \tag{41}$$

where σ_u represents the standard deviation of the gust velocity, L_u is the scale height, V is the mean wind velocity, and ω is the circular frequency in rad/s [48].

From the spectrum in Equation (41), time histories can be generated that encompass the necessary statistical characteristics. To generate time histories, the von Karman Continuous Wind Turbulence Model within the Simulink Aerospace Blockset was used. This block passes white noise through a filter designed to produce velocity spectra consistent with the von Karman spectrum [49]. The white noise used is band-limited with a unit variance. Several input parameters are required, including low altitude intensity defined by the wind speed at 20 ft, wind direction at 20 ft, turbulence intensity, scale height, time step, wingspan, altitude, and seed numbers for the white noise generation [49]. As described in Military Specification MIL-F-8785C [50] and Military Handbook MIL-HDBK-1797 [51], the turbulence scale height and intensity has been divided into two distinct regions, each a function of the altitude. For low altitudes—below 1000 ft—the intensity is a function of the wind velocity at 20 ft (W_{20}). Typically, for light, moderate, and severe turbulence W_{20} is taken to be 15, 30, and 45 knots, respectively. The equation for the intensity, σ_u, then is as [49]

$$
\sigma_w = 0.1 W_{20},
$$
$$
\frac{\sigma_u}{\sigma_w} = \frac{1}{(0.177 + 0.000823h)^{0.4}},
$$

$$(42)$$

where h is the altitude in feet. The scale height for low altitude turbulence is similar.
Specifically,

$$L_u = \frac{h}{(0.177 + 0.000823h)^{1.2}}. \tag{43}$$

Altitudes above 2000 ft have a constant scale length $L_u = 2500\ ft$. Turbulence

intensity for this region is generated from a lookup table based on the altitude and

probability of the turbulence intensity being exceeded. For altitudes between the

1000 and 2000 ft, the values are linearly interpolated [49]. The Simulink block

diagram of the turbulence model is included below in Figure 6-1.
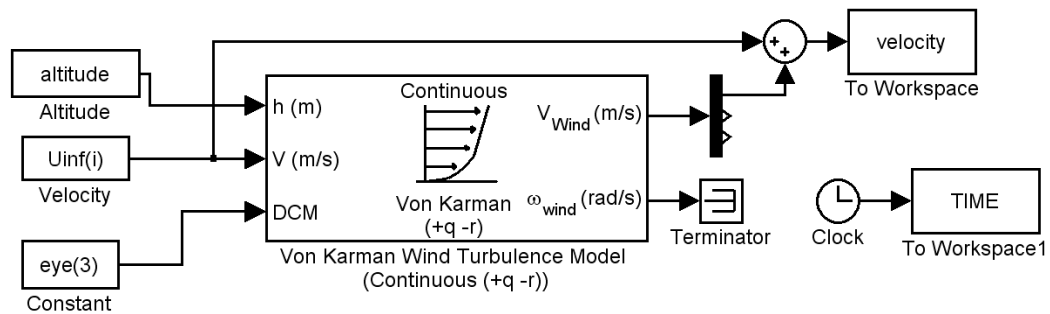
Figure 6-1: Simulink Block Diagram of Turbulence Generation

6.2. Application

Using the numerical integration framework from Chapter 4, a similar model

was developed. The process is exactly the same as in Figure 4-2, except the velocity

used in the calculation of the aerodynamic forces is sampled from a stochastic time

history generated by the Simulink turbulence model previously described.

Chapter 7

Results and Discussion

By coupling the quasi-steady aerodynamic model and structural model

derived above, numerical analysis was performed within Matlab. The computations

were run on an Intel Core2 2.40GHz processor with 3GB RAM. The time step chosen

for updating the aerodynamic forces was chosen to be $\Delta t = \frac{c}{5000}$. This was done

based on the step size chosen in Reference [27]. In that paper the authors chose a

step size of $\Delta t = \frac{c}{100V}$. No qualifications were given for this expression, but based on

the results presented in their paper was found to be adequate. The removal of the

velocity dependency was done to remove any potential variations in the data due to

different sampling times at different velocities. The structural equations of motion

were integrated in time while the aerodynamic forces were updated at each

iteration using this time step. Using this time step the simulations for the constant

velocity case took roughly 30 minutes to compute 60 seconds of data. With the

added complexity of generating the stochastic velocity time history the stochastic

simulations averaged roughly four hours and 20 minutes to compute 60 seconds of

data. The large difference between the two methods results from having to compute

the stochastic velocity time history, save it to a file, and then read in values at every

iteration. Accessing data in other files is very time consuming.

7.1. Quasi-steady Aerodynamics with Constant Velocity

A range of flow velocities was used to determine the velocity at which the

oscillations might become detrimental to the craft. Figure 7-1 and Figure 7-2, below,

show the pitch and plunge displacement as a function of time. Note the different

time scales on the two figures. As the velocity is increased, the aerodynamic effects

cause the damping to decrease resulting in a longer settling time. In Figure 7-1 the

displacements have both settled after only a little more than 4 seconds whereas in

Figure 7-2 it takes nearly a minute.

As the velocity increases past 87 m/s the behavior becomes very lightly

damped until at 89 m/s the behavior depicted in Figure 7-3 is seen. It was found

that air velocities below approximately 89.2 m/s either damped out or were
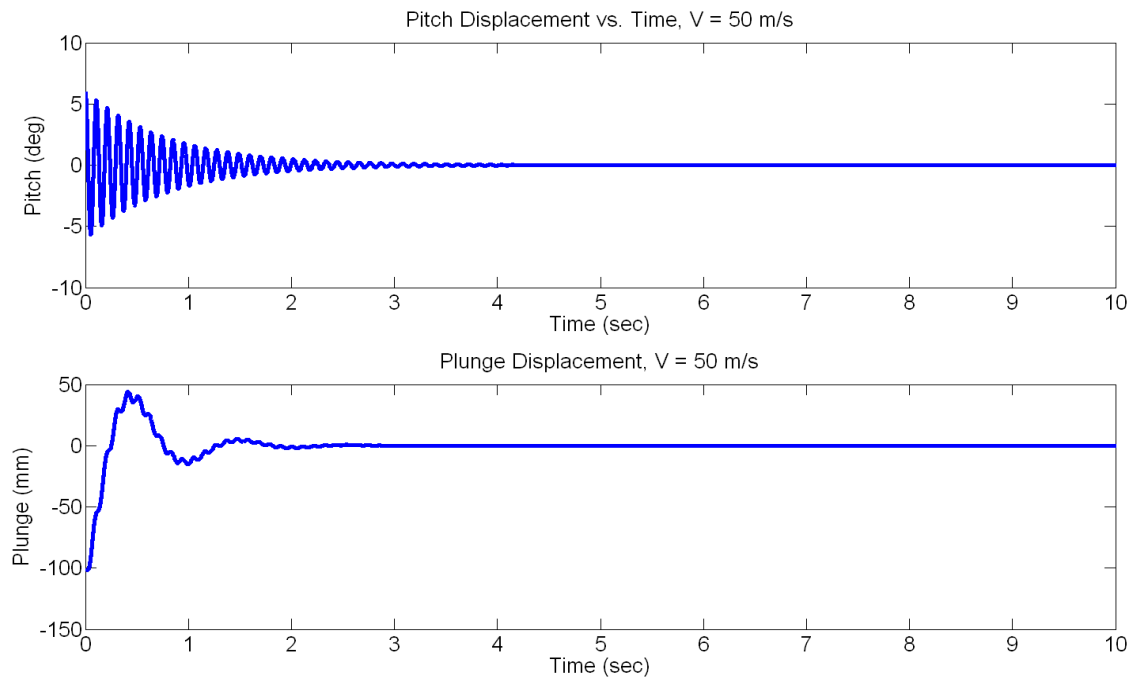
sustained at constant amplitude.

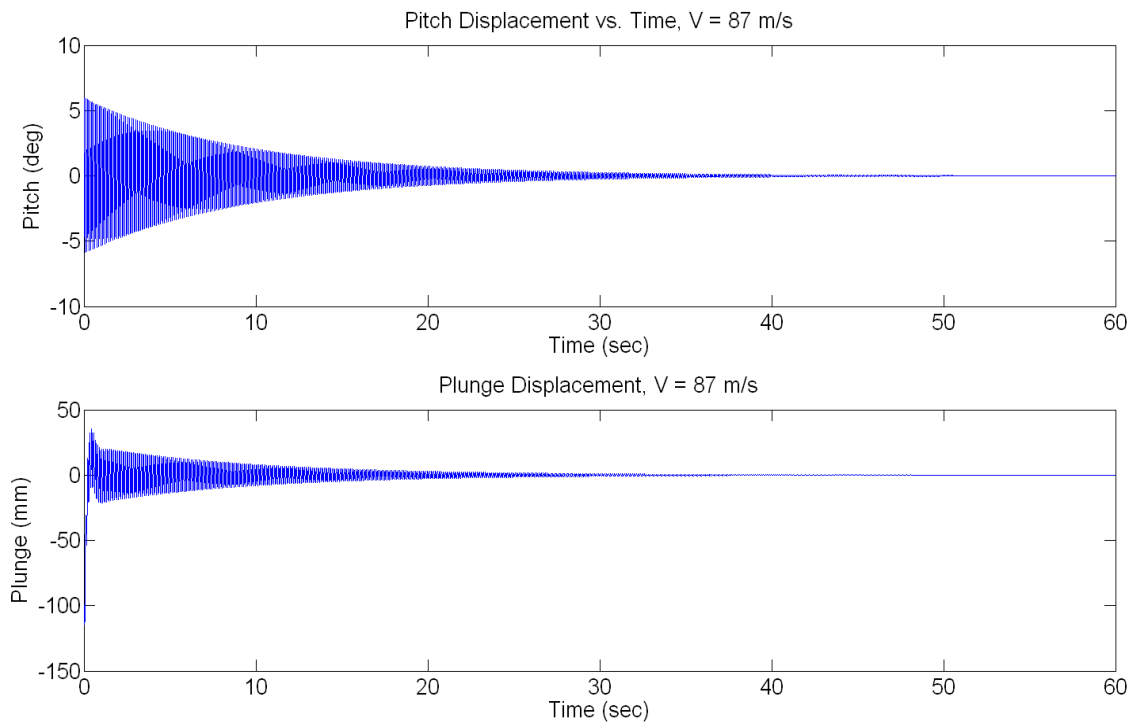**Figure 7-1: Pitch and Plunge vs. Time, V = 50 m/s**

Figure 7-2: Pitch and Plunge vs. Time, V = 87 m/s

Pitch Displacement vs. Time, V = 89 m/s
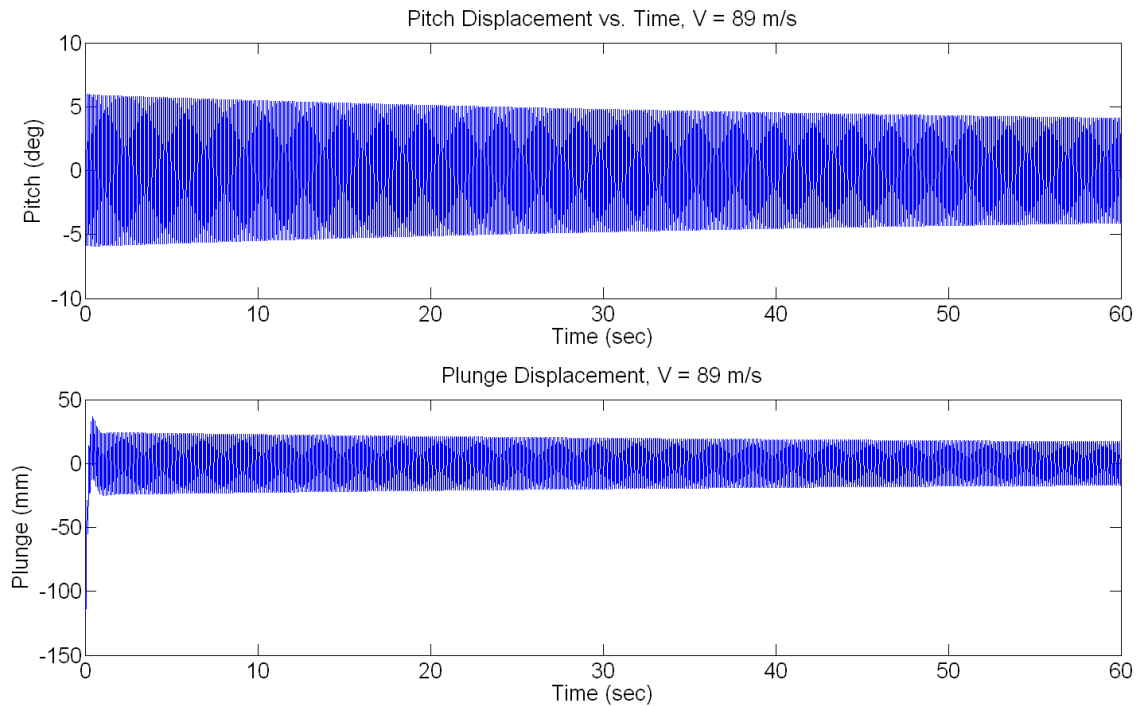
Plunge Displacement, V = 89 m/s

Figure 7-3: Pitch and Plunge vs. Time, V = 89 m/s

For velocities larger than 89.2 m/s, the oscillations increased to a bounded steady state limit cycle oscillation. Again the settling time was dependent on the velocity however in the opposite sense it had before; higher velocities reached steady-state oscillations faster than those closer to the critical velocity. This behavior can be seen in Figure 7-4 and Figure 7-5. Both figures have the same time scale. Figure 7-4 does not approach steady-state amplitude until approximately 60 seconds whereas Figure 7-5 takes just over 10 seconds.
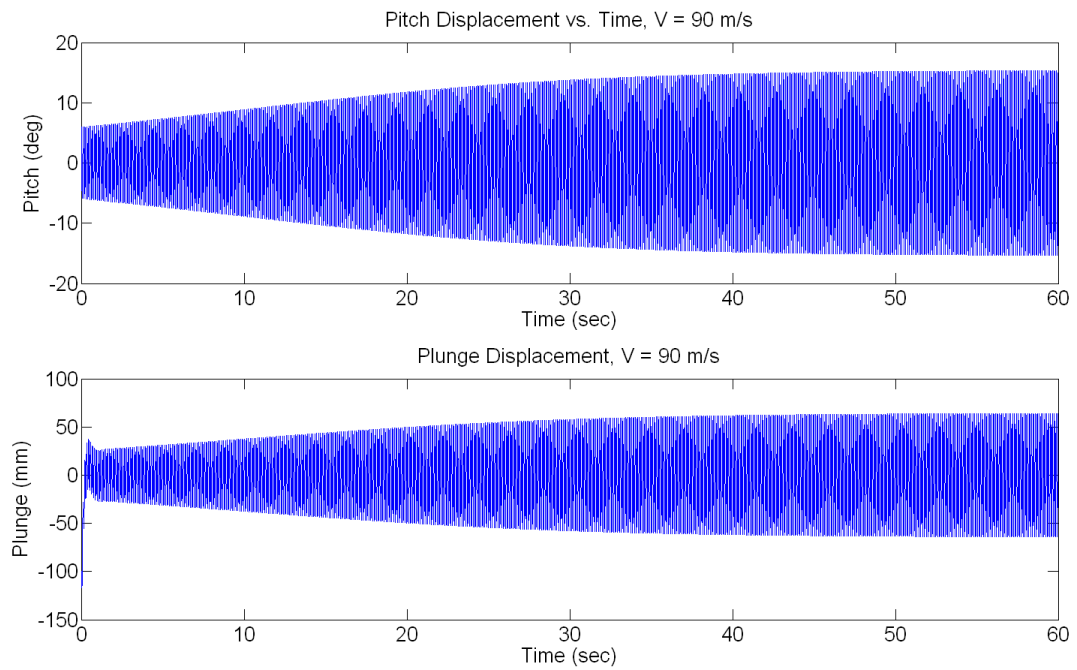
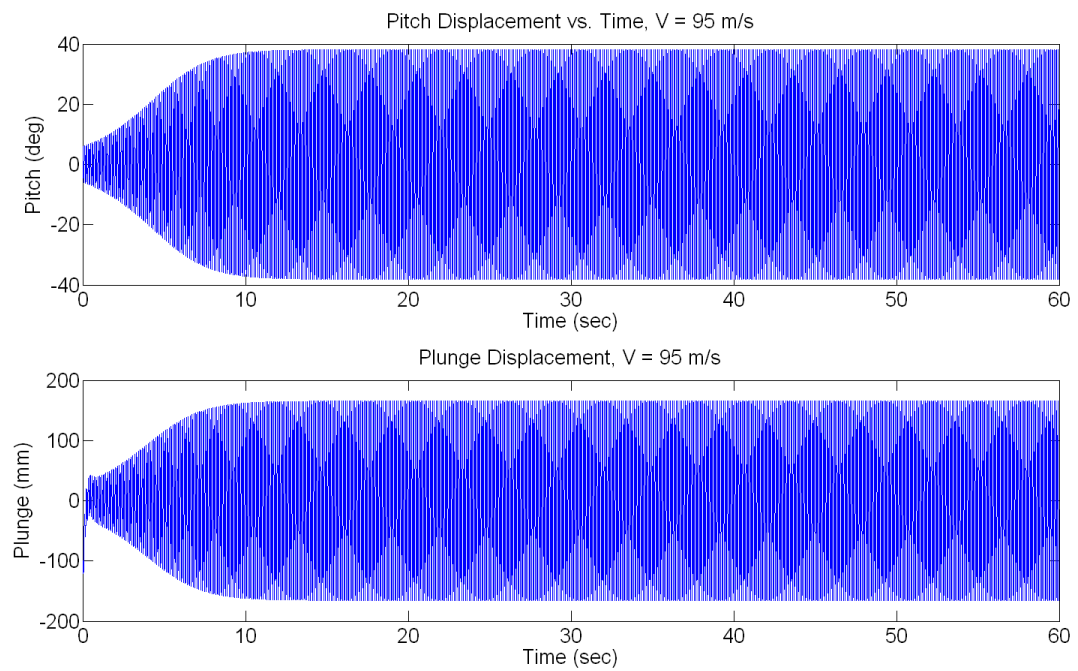**Figure 7-4: Pitch and Plunge vs. Time, V = 90 m/s**

Figure 7-5: Pitch and Plunge vs. Time, V = 95 m/s

Note that the amplitude of the angle of attack oscillations is beyond the linear region for which the analysis scheme used applies. However, this behavior cannot be corrected for without an appropriate dynamic stall model.

From Table 2-1, the cruise velocities for the HALE UAVs ranged from approximately 60-175 m/s. While the representative model analyzed herein was not meant to match any of the HALE UAVs in Table 2-1, the model did incorporate various aspects common among them. The critical velocity of approx. 89.2 m/s is encompassed by the range given in Table 2-1. From this one might argue that the analysis holds some realism even given the numerous simplifying assumptions.

As the velocity increases past the onset of LCO, the amplitude of the LCO also increases. Figure 7-6 shows how the amplitude changes with the velocity. A trend between the lift force amplitude and plunge amplitude is evident, and the same can be said for the moment and the angle of attack. The data also appear to have an asymptotic relationship with the critical velocity which is noted by the red dashed line. Further, the amplitudes appear to change linearly as the velocity increases past approximately 95 m/s.
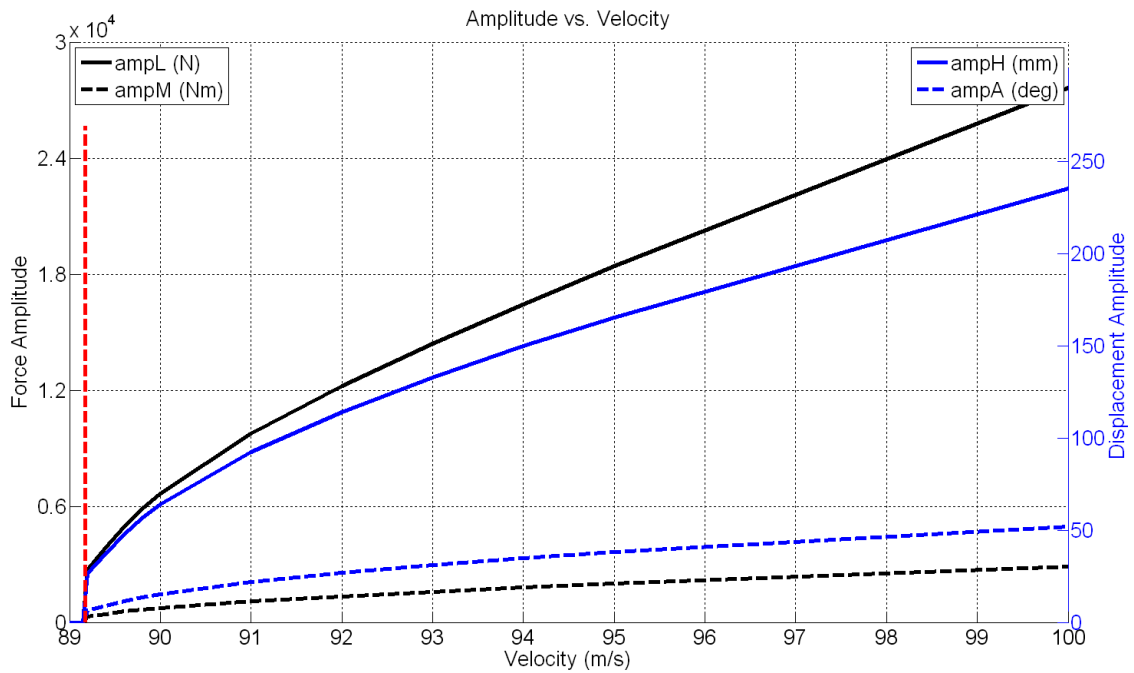
Figure 7-6: Aerodynamic Force and Displacement Amplitude as a Function of the Velocity

Figure 7-7 presents the frequency of oscillation as a function of the velocity. A red dashed line represents the critical velocity found earlier. Although the frequency variation in the figure is quite small (less than one rad/s variation) there is a distinct corner located at the critical velocity. Further, note how similar the frequencies of the aerodynamic forces and structural displacements are. This is not too surprising as the aerodynamic forces are directly dependent on the angle of attack, and the angle of attack is also dependent on the aerodynamic forces. It is pointed out that the data used in Figure 7-7 are not calculated to reach steady-state; only 60 seconds of data was simulated. For the post-critical velocity simulations, the steady-state behavior was reached in the form of LCO. However, with the

computational resources used and the necessary length of data required to reach

steady state for velocities just prior to the critical velocity, the requisite computation

time was prohibitive for this study. Additionally, no effort was made to optimize the

time step so as to achieve an acceptable accuracy with minimal computation time.
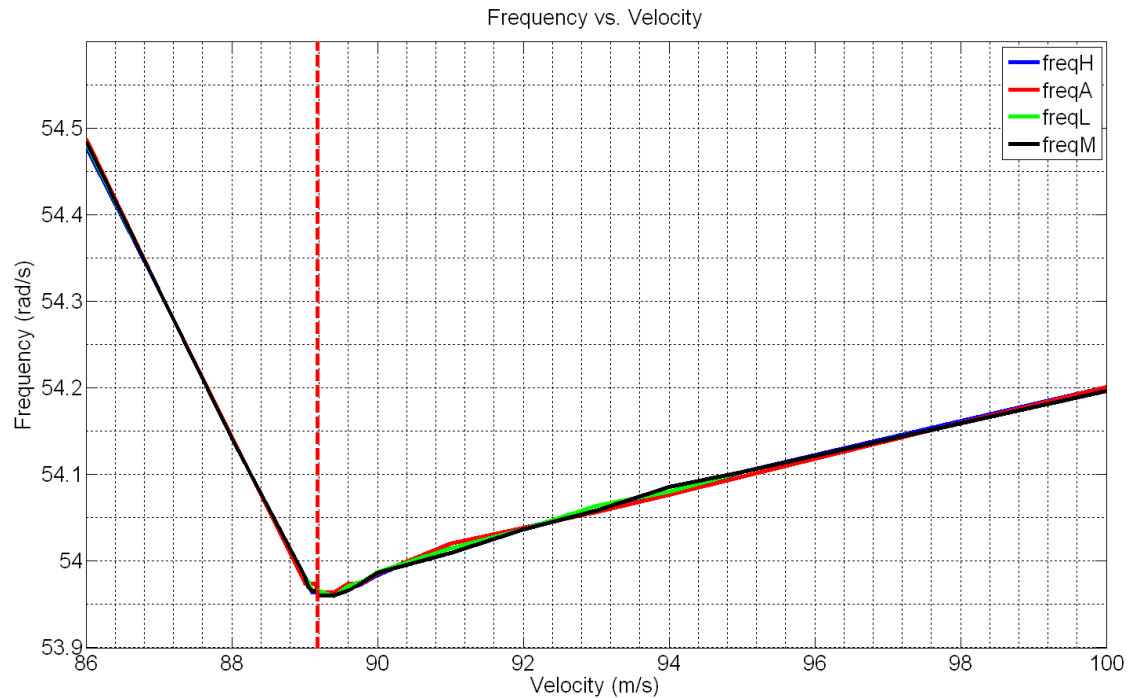

Figure 7-7: Frequency of Oscillation as a Function of Velocity

Figure 7-1 through Figure 7-7 show the aeroelastic behavior of the system,

but the cause of such behavior is also relevant. Using the same model, behavior at

velocities much smaller than the critical velocity was simulated. Figure 7-8 shows

the behavior at 10 m/s. The frequencies of the pitch and plunge oscillations are

distinctly different. An interesting phenomenon is encountered as the velocity is
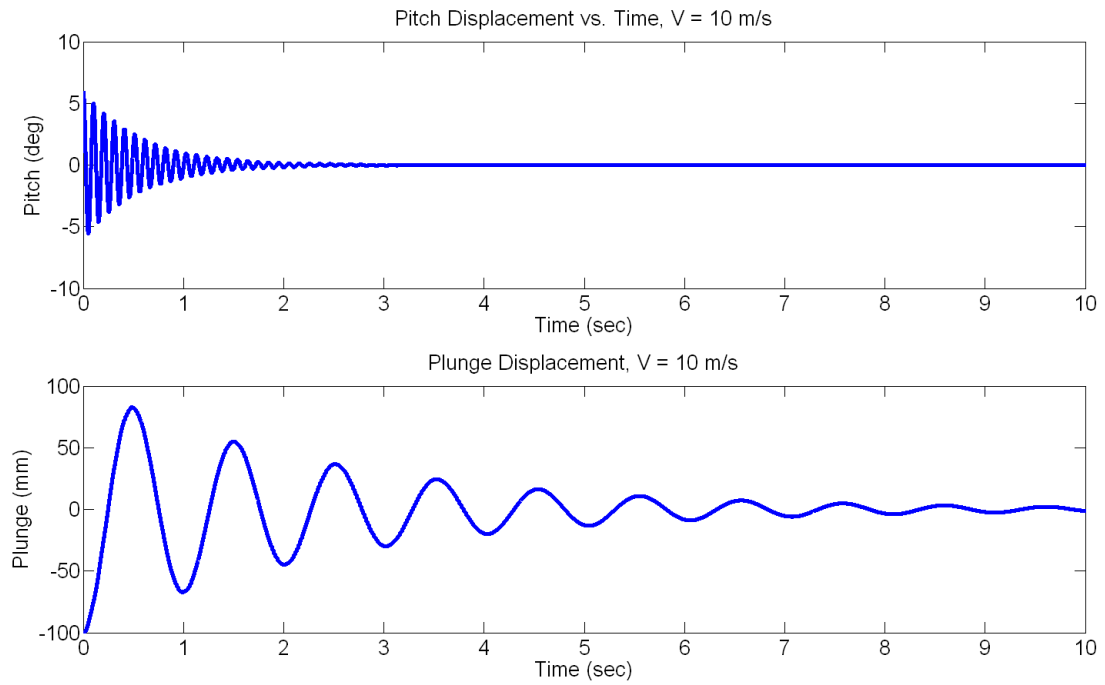
increased.

Figure 7-8: Pitch and Plunge vs. Time, V = 10 m/s

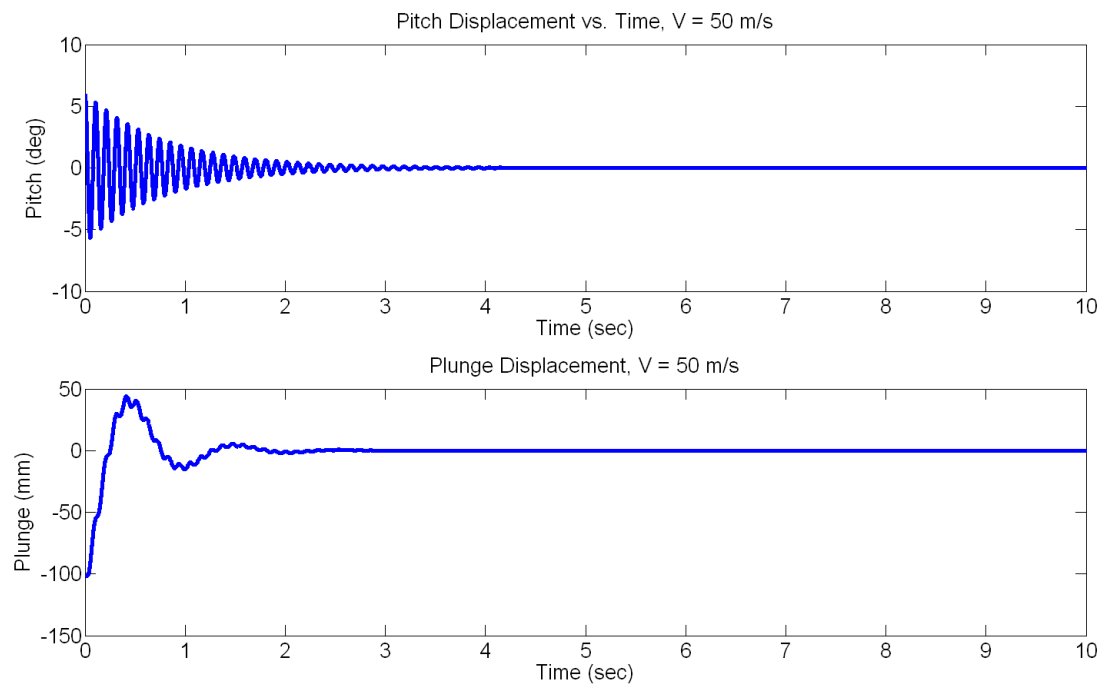**Figure 7-9: Pitch and Plunge vs. Time, V = 50 m/s**

As Figure 7-9 shows, at 50 m/s the pitch amplitude begins at approximately the same amplitude, yet is not damped out as quickly. This is consistent with the previously mentioned displacement figures; the damping decreases with increasing velocity. However, note the drastic change in the plunge displacement. The initial amplitude peak has reduced in amplitude and the damping has actually increased. Further, a secondary frequency has become apparent. Further increases in the velocity make this secondary frequency more prominent. Figure 7-10 shows the displacements at 80 m/s. The secondary frequency in the plunge displacement appears to have become dominant. Similarity to the pitch frequency is also noted. An additional increase in the velocity to 90 m/s shows a continuance of this behavior.
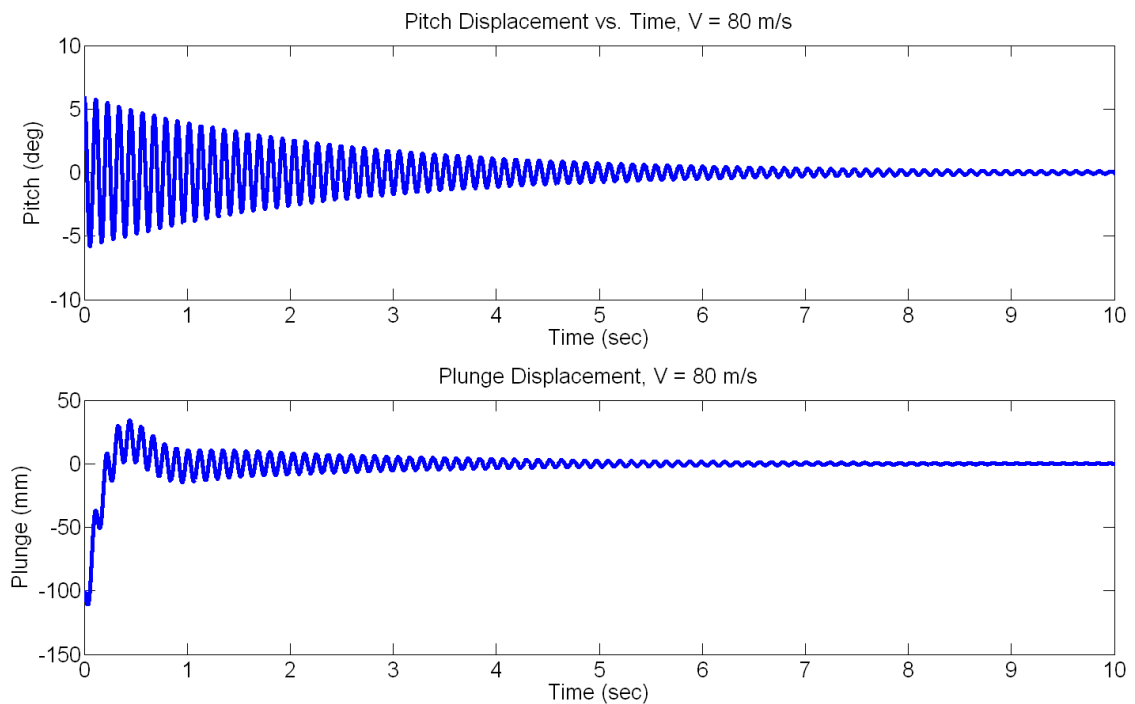

Figure 7-10: Pitch and Plunge vs. Time, V = 80 m/s

However, as Figure 7-11 shows, 90 m/s is past the critical velocity and LCO behavior has started to occur. One explanation for the emergence of LCO is the coalescence of the pitch and plunge frequencies. When the velocity is very low, the pitch and plunge modes are fairly independent of each other. As the velocity increases the plunge frequency becomes more and more dependent on the pitch frequency. This is expected as the lift and moment forces are a function of the pitch angle. The behavior shown here is indicative of the flutter mechanism described by Figure 1-1.
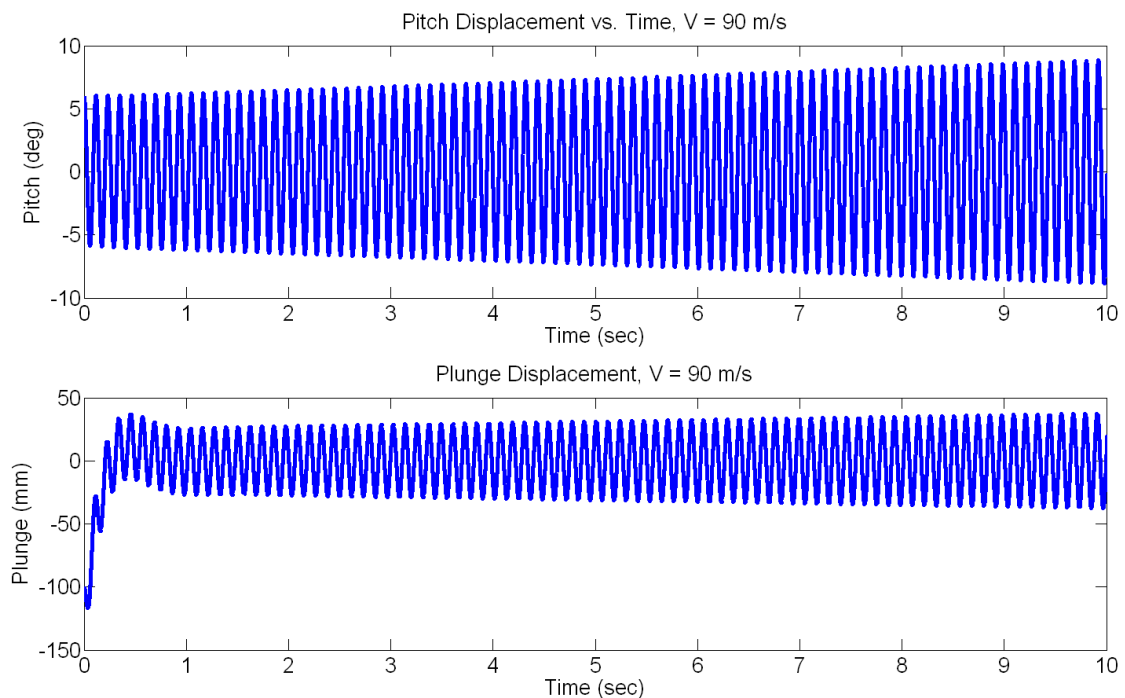

Figure 7-11: Pitch and Plunge vs. Time, V = 90 m/s

Furthermore, classical flutter analysis has found that if dynamic stall were taken into account, one might expect the high frequency of the pitch velocity to result in

separated flow (stall) and thus decreased aerodynamic forces. The resulting

behavior would likely appear differently than shown here.

7.2. Harmonic Balance

From the harmonic balance formulation described previously, a computer

model was developed within the Matlab environment. Forcing data from the quasi-

steady numerical integration model was fit to a single harmonic of the form:

$$F = Asin(\omega t) + Bcos(\omega t) \tag{44}$$

Using the *fit* command in Matlab, the parameters *A, B,* and ω were calculated for

both the aerodynamic lift and moment based on the forcing data obtained from the

numerical integration. The *fit* command in Matlab uses a nonlinear least squares

method to fit the data to a first order Fourier series expansion. The coefficient of

determination is of the order 0.99999. Figure 7-12 below shows the superposition

of the forcing data and the resulting first order Fourier series. This case was done

for a velocity of 90 m/s. The time scale was modified to accurately show the

agreement. Parameters, *A, B,* and ω for both the lift and moment were then input

into the nonlinear harmonic balance solver. The goal of this analysis is to attempt to

predict the steady-state oscillation amplitude and frequency if the amplitude and
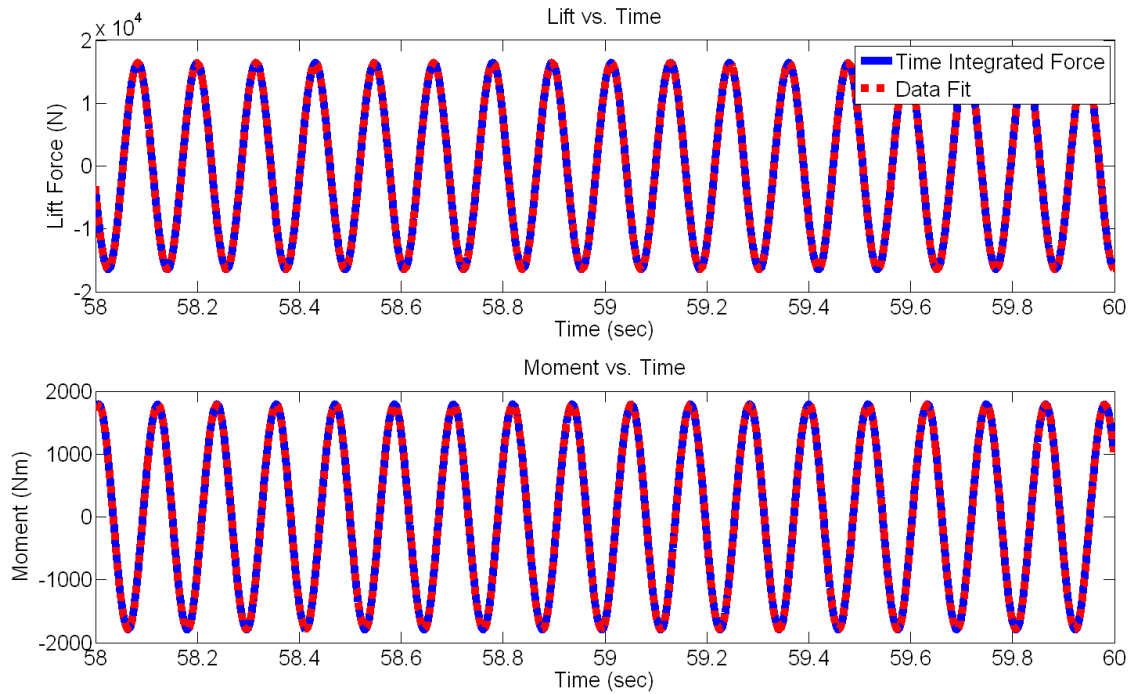
frequency of the forcing is known.

Figure 7-12: Aerodynamic Forces Fit to 1st Order Fourier Series

Using the harmonic balance solver developed in section 5.1, the harmonic

forcing data for each velocity was input in terms of the amplitudes and frequency of

oscillation. From this, the solver computed the coefficients of the assumed response

used from Equation (34). For a velocity of 90 m/s, the results are shown in Figure
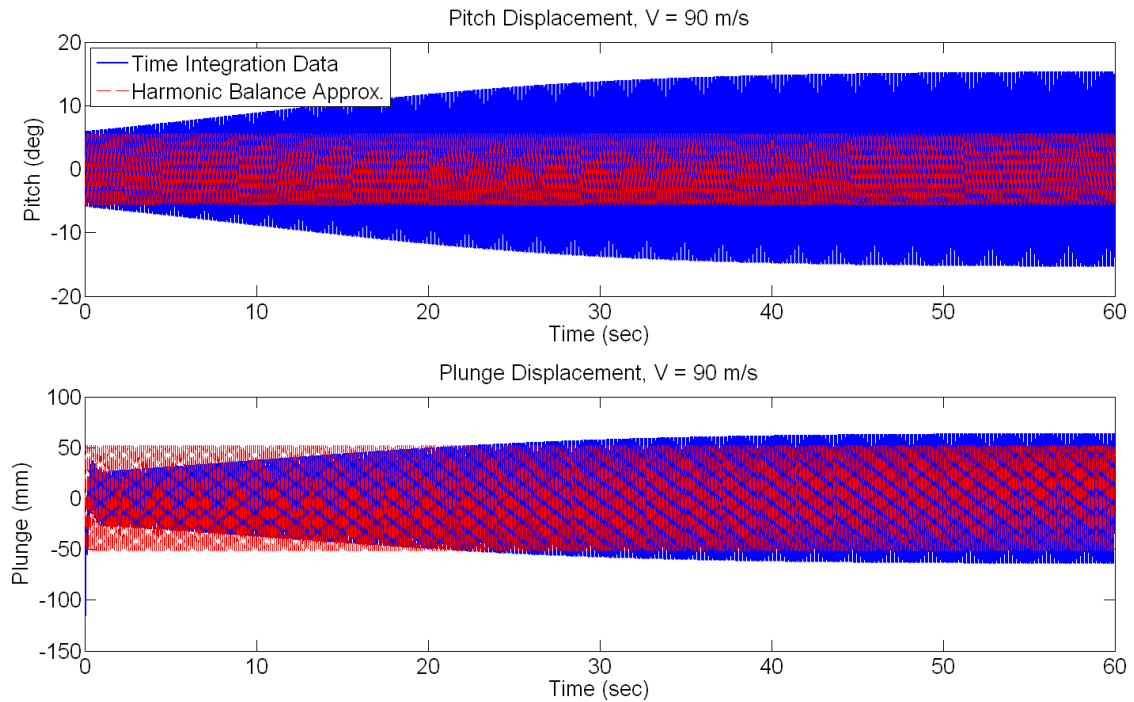
7-13.

Figure 7-13: Harmonic Balance Model, V = 90 m/s

The behavior is not as expected. For the pitch displacement the harmonic balance approximation is very good initially, but then the amplitude diverges to approach the LCO amplitude. For the plunge displacement the behavior is almost the opposite; initially the approximation is poor but approaches the LCO amplitude much better than the pitch degree of freedom. There appears to be some mechanisms at work that prevent the harmonic balance from properly predicting the steady-state oscillatory behavior. Presently these mechanisms are unknown and require additional investigation to determine the cause of the disagreement. Some areas for further examination include the implementation of the equations of motion within the numerical integration model, the coding of the harmonic balance

model, or possibly the addition of the aerodynamic forcing on the structure. With respect to frequency agreement, Figure 7-14 shows a rather close match. Frequency agreement was seen at all velocities for both degrees of freedom. This is not surprising, however, as the displacement frequency is directly related to the forcing frequency.
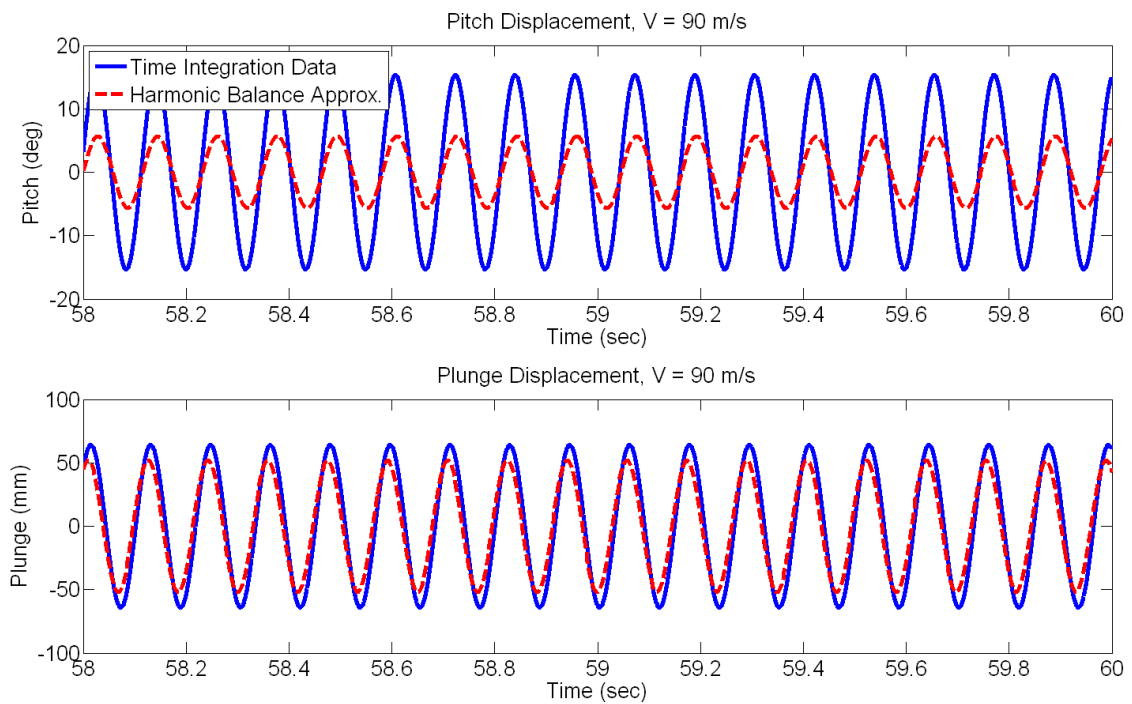

Figure 7-14: Harmonic Balance Model, V = 90 m/s (Zoomed in)

For larger velocities the initial agreement in the pitch displacement is not present as seen in Figure 7-15and Figure 7-16. However, in the plunge degree of freedom the harmonic balance approximation approaches the time integration results as velocity is increased. A similar trend is seen in the pitch degree of freedom but is not as apparent.
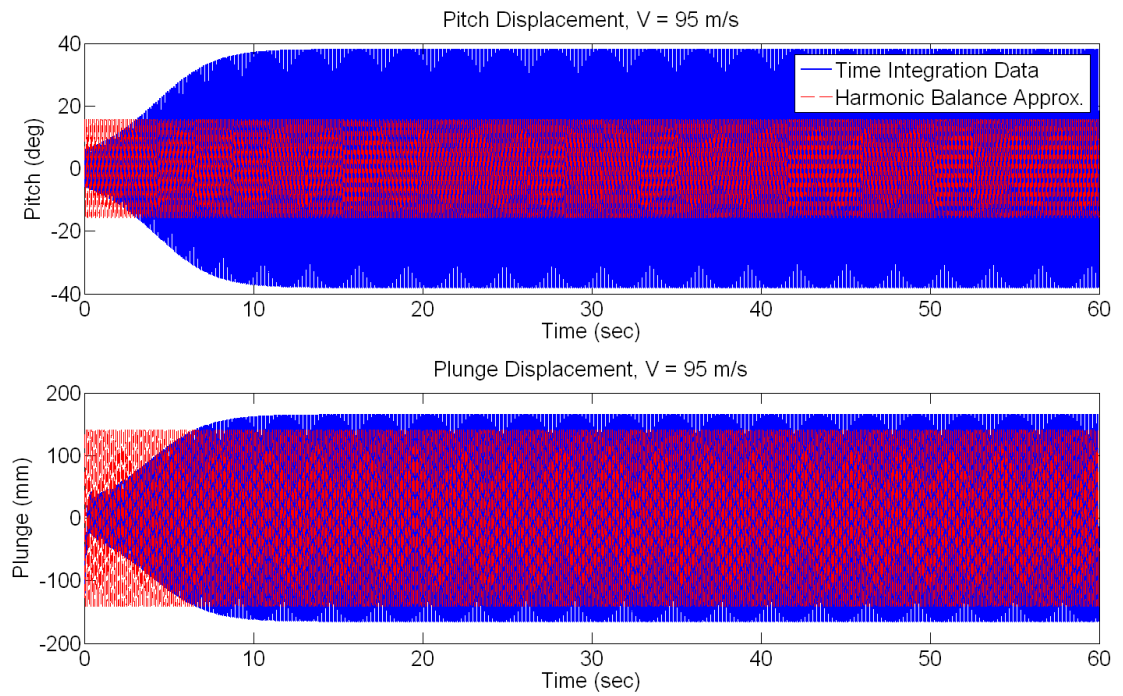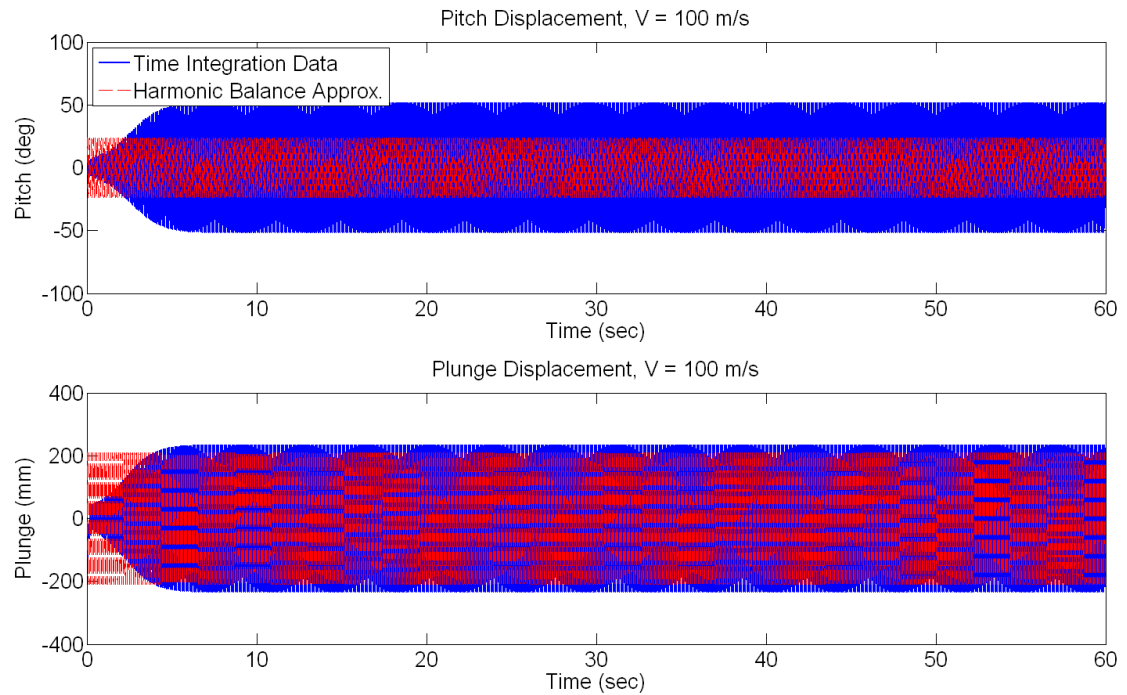
Figure 7-15: Harmonic Balance Model, V = 95 m/s

Figure 7-16: Harmonic Balance Model, V = 100 m/s

For a small range of post-critical velocities Figure 7-17 shows how the error changes with respect to velocity. The error is calculated by the equation

$$\% \, Error = \frac{|HB - TI|}{TI} * 100, \tag{45}$$

where HB is the magnitude of the harmonic balance approximation and TI is the magnitude of the time integration data. A linear relationship is seen that has the same rate of change for both the pitch and plunge degrees of freedom. As the figure shows, however, the rate of change is very gradual. The pitch degree of freedom would require very high velocities that are unreasonable for such an aircraft as modeled herein to reach agreement using this trend.
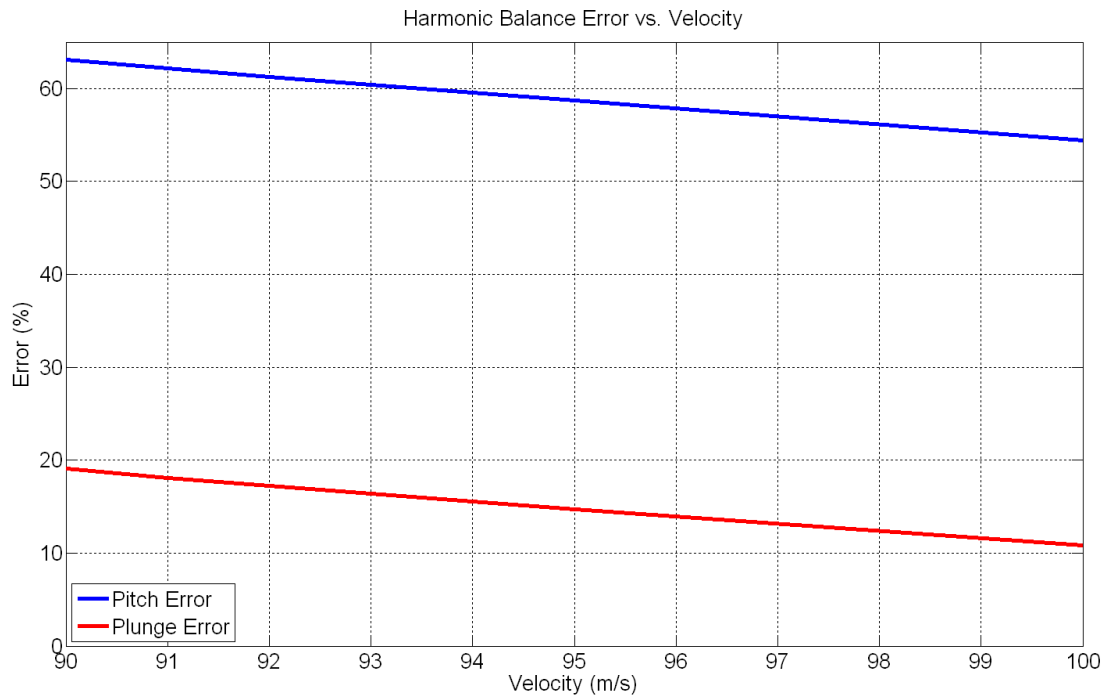

Figure 7-17: Harmonic Balance Approximation Error as a Function of Velocity

7.3. Quasi-steady Aerodynamics with Stochastic Velocity

Using a stochastic velocity input based on the von Karman spectrum, the results are similar, yet display the sensitivity of the system to variations in the velocity. Within the von Karman turbulence model the turbulence intensity was taken to be severe. Figure 7-18, Figure 7-19, and Figure 7-20 show the pitch and plunge generated by stochastic velocity inputs. The stochastic velocity time histories are shown in the center plots in each figure. A red dashed line in the center plot also represents the critical velocity found previously. In Figure 7-18 the mean velocity is below the critical velocity and thus based on the results presented above one would expect the displacements to damp out to zero eventually. But, when the variability of the wind turbulence is taken into account, the velocity contains periods both above and below the critical velocity. When the critical velocity is exceeded, the displacements show behavior similar to LCO. When the velocity later decreases below the critical velocity the displacements converge to zero as one would expect. The same behavior is seen in Figure 7-19, where the mean velocity is right at the critical velocity. In Figure 7-20 where the mean velocity is above the critical velocity, the displacements vary as in the previous two figures. However, as the velocity is almost exclusively above the critical velocity, the displacements merely vary between LCO of different amplitude.
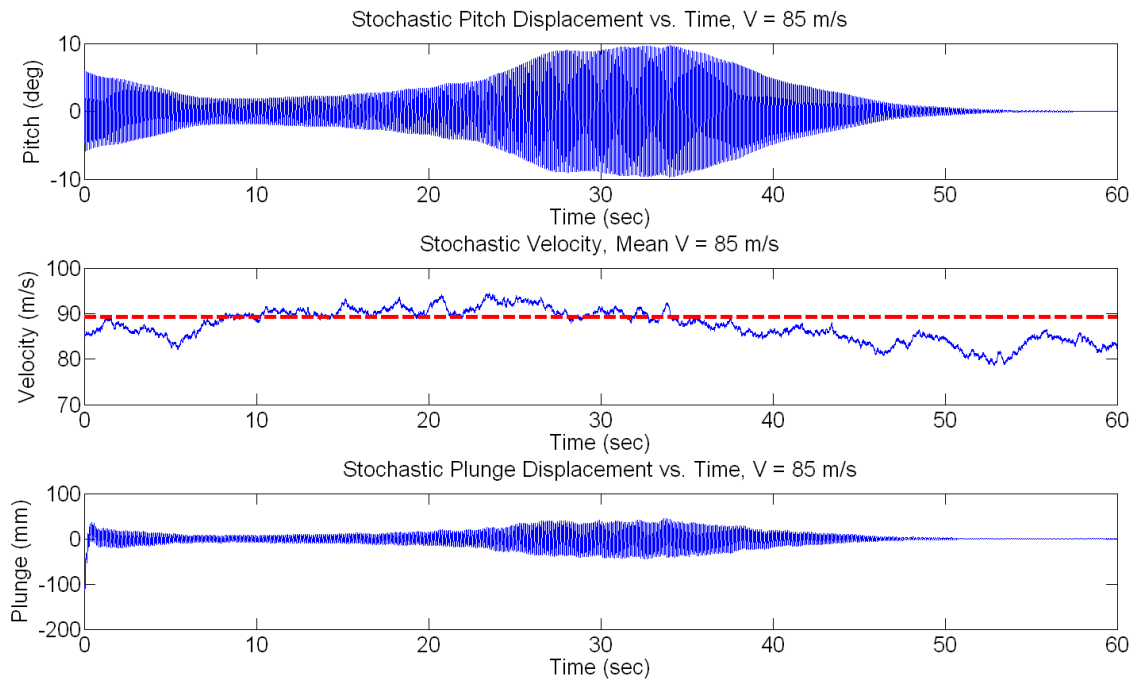
Figure 7-18: Pitch and Plunge vs. Time with Stochastic Velocity Input, Mean Velocity = 85 m/s
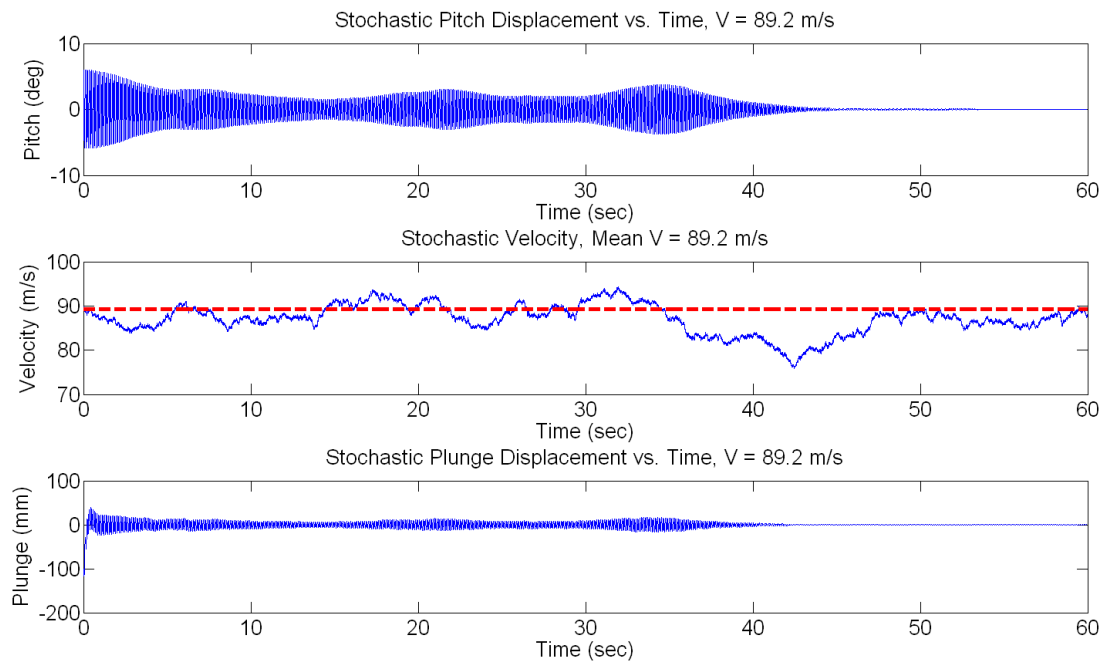

Figure 7-19: Pitch and Plunge vs. Time with Stochastic Velocity Input, Mean Velocity = 89.2 m/s
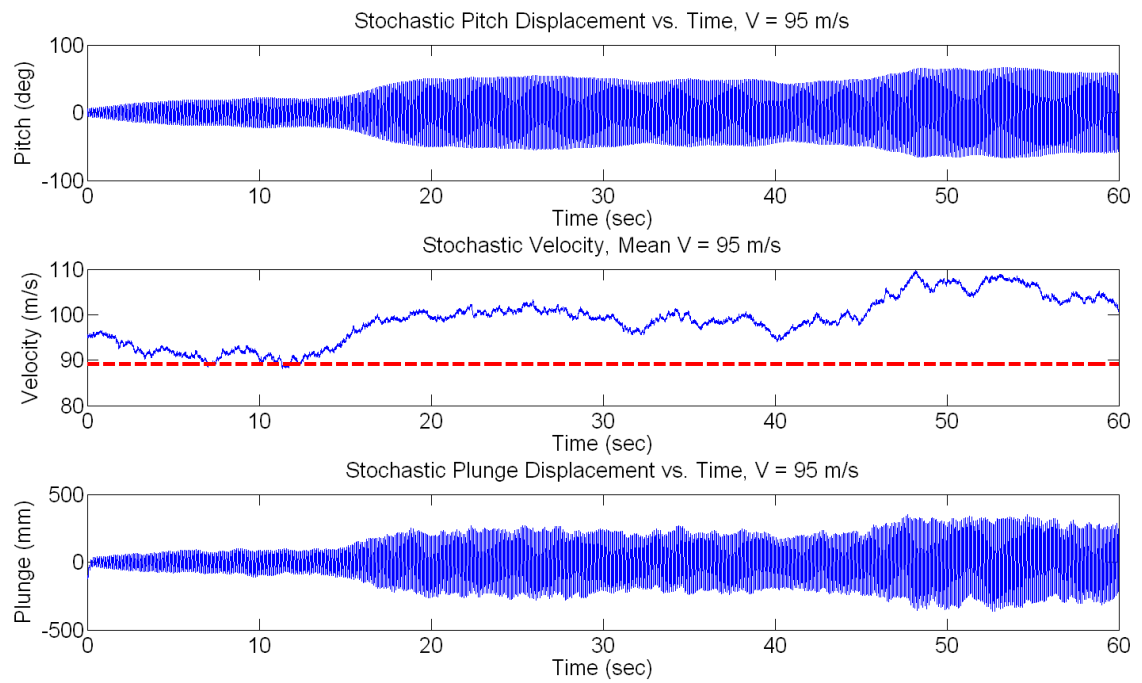
Figure 7-20: Pitch and Plunge vs. Time with Stochastic Velocity Input, Mean Velocity = 95 m/s

Chapter 8

Concluding Remarks

The relative inexpensive nature of UAVs lends itself towards inexpensive methods of analysis—both monetarily and computationally—as well as inexpensive test vehicles. If such cost savings could be realized, the utilization of UAVs would grow in leaps and bounds. Improved analysis techniques would allow designers and engineers to spend more time and effort on other challenges which would open the door to new and exciting technologies.

To that end, the goal of this thesis has been to determine the applicability of modeling post-critical flutter behavior via the harmonic balance method as well as to examine the effects of stochastic forcing. As aircraft design and analysis is an expensive endeavor, any means by which costs can be reduced are beneficial. The harmonic balance has been an attempt to reduce the costly process of numerical integration of the equations of motion. Numerical integration is a great tool for

simple systems, however as complexity is added in the structure or force model the feasibility of accurate numerical results becomes much more costly in terms of time and computational resources. To avoid this cost, it was hoped that the LCO could be accurately modeled by knowing the applied harmonic forcing. Based on the findings herein, the applied forcing was found to be harmonic once LCO was achieved. Using this forcing the frequency of oscillation for both pitch and plunge displacement has been modeled quite closely. Amplitude, on the other hand, was off by as much as almost 63%. Some possible areas of discrepancy here might include the choice to neglect the unsteady effects or perhaps lack of a dynamic stall model. The only conclusion that can be made at this time concerning the applicability of the harmonic balance method is that more investigation is needed.

In examining the effects of stochastic forcing on aeroelastic behavior the results were rather expected. Velocities below the critical value are damped out at different rates depending on the magnitude of the velocity. Exceeding the critical velocity, on the other hand, results in LCO. One major finding from this study, however, is that there exists a range of notable velocities around the critical velocity. The width of this range depends on the turbulence intensity. In essence this creates a buffer zone around the critical velocity which should be avoided when operating in turbulent conditions.

Although this analysis is considerably simplified and contains many areas for improvement, the insights garnered here are quite useful. Baseline characteristics

have been observed that can be improved through incorporating additional model components that better represent the physics of the real world problem.

8.1. Future Work

Based on the findings of this work, there are several opportunities for further study. Aerodynamic modeling stands as the greatest opportunity to improve the results gained from this analysis. Incorporating a fully unsteady aerodynamic model would increase the realism of the analysis by including wake and inertial effects. Several models have been proposed based on the work of Theodorsen [36] and Wagner [37]. Beddoes [52] has also developed a computationally efficient model for use in rotor analysis based on an indicial formulation. Including these more advanced models would likely increase the requisite computation time. However, perhaps the additional aerodynamic considerations would lead to better agreement between the harmonic balance method and the time integration results. Extending the harmonic balance formulation to more than one harmonic excitation might also result in better agreement.

The angle of attack results presented herein exceeded the region where the linear lift curve slope applies. Accordingly, worthwhile model improvements should also contain some type of dynamic stall model. Perhaps this entails simply fitting a polynomial to the lift curve to capture the dynamics at higher angles of attack, or perhaps requires building on previous work by Leishman and Beddoes [53] or McAlister, et al [54].

Further investigation into the stochastic effects is also worthwhile. Employing a stochastic linearization approach [55] might reveal additional important characteristics of the aeroelastic problem within the framework of turbulent aerodynamics.

Another major area of possible improvement is to look at the aeroelastic behavior of an entire finite wing. As mentioned before, many researchers have spent considerable effort in developing complex finite element models of entire aircraft which are then coupled to unsteady aerodynamics code. By refining the number of elements, higher order vibration modes can be modeled which can also contribute to the frequency coalescence shown previously. Further, better accuracy in the displacements can be achieved with higher order models than with the simple 2nd order model analyzed herein. Taking into account three-dimensional effects is also an avenue for improvement.

In terms of the simulation presented, computation time improvements can also be made by finding an optimal time step which gives accurate results and minimal computation time. Further, the code can be perhaps modified to run in parallel with a multi-node system. Stochastic velocity time histories could also be generated via auto-regressive (AR) [56] or auto-regressive moving-average (ARMA) [57] algorithms . Perhaps this would speed up the stochastic modeling.

References

[1]   R. Bisplinghoff, H. Ashley, and R. Halfman, *Aeroelasticity*. Addison-Wesley Professional, 1955.

[2]   D. Hodges and A. Pierce, *Introduction to Structural Dynamics and Aeroelasticity*. Cambridge, UK: Cambridge University Press, 2002.

[3]   Y. C. Fung, *An Introduction to the Theory of Aeroelasticity*. New York, NY: John Wiley & Sons, 1955.

[4]   T. Weisshaar, "Static and Dynamic Aeroelasticity," *Encyclopedia of Aerospace Engineering*. John Wiley & Sons, 2010.

[5]   S. Brandt, R. Stiles, J. Bertin, and R. Whitford, *Introduction to Aeronautics: A Design Perspective*, 2nd ed. Reston, VA: AIAA, 2004.

[6]   R. Clark, D. Cox, H. C. Curtiss, J. Edwards, K. Hall, D. Peters, R. Scanlan, E. Simiu, F. Sisto, and T. Stragnac, *A Modern Course in Aeroelasticity*, 4th ed. Dordrecht, The Netherlands: Kluwer Academic Publishers, 2004.

[7]   J. B. Kosmatka and J. Panza, "Aeroelastic Analysis of a Composite UAV," presented at the 43rd AIAA/ASME/ASCE/ASC Structures, Structural Dynamics, and Materials Convention, Denver, CO.

[8]   S. Munteanu, J. Rajadas, C. Nam, and A. Chattopadhyay, "Quasi-Linear Approach for Solving Aeroelastic Problems Involving Aerodynamic and Structural Nonlinearities," presented at the 44th AISS/ASME/ASCE/AHS Structures, Structural Dynamics, and Materials Conference, Norfolk, VA, 2003.

[9]   L. Demasi and E. Livne, "Aeroelastic Coupling of Geometrically Nonlinear Structures and Linear Aerodynamics: Two Formulations," *Journal of Fluids and Structures*, vol. 25, pp. 918–935, 2009.

[10] F. Kachra and S. K. Nadarajah, "Aeroelastic Solutions Using the Nonlinear Frequency-Domain Method," *AIAA Journal*, vol. 46, pp. 2202–2210, Sep. 2008.

[11] M. Patil, D. Hodges, and C. Cesnik, "Characterizing the Effects of Geometrical Nonlinearities on Aeroelastic Behavior of High-Aspect-Ratio Wings," presented at the International Forum on Aeroelasticity and Structural Dynamics, Williamsburg, VA, 1999.

[12] L. Demasi and E. Livne, "Dynamic Aeroelasticity of Structurally Nonlinear Configurations Using Linear Modally Reduced Aerodynamic Generalized Forces," *AIAA Journal*, vol. 47, pp. 71–90, Jan. 2009.

[13] National Research Council, *Uninhabited Air Vehicles: Enabling Science for Military Systems*. Washington, D.C.: National Academy, 2000.

[14] J. R. Wilson, "Unmanned and Airbourne: A New Plan," *Aerospace America*, no. 24, Mar-2010.

[15] A. Noor and S. Venneri, *Future Aeronautical and Space Systems*. Reston, VA: AIAA, 1997.

[16] H. Fiemelt, "Some Consequences of UAV Design Requirements Especially on UAV Modeling and Simulation," *AIAA*, 2003.

[17] M. Figat and T. Goetzendorf-Grabowski, "Aerodynamic Calculation of Unmanned Aircraft," in *Aircraft Engineering and Aerospace Technology*, vol. 77.6, 2005, p. 467–74.

[18] Ko, Jeonghwan, Andrew J. Kurdila, and Thomas W. Strganac. "Nonlinear Control of a Prototypical Wing Section with Torsional Nonlinearity." *Journal of Guidance, Control, and Dynamics* 20.6 (1997): 1181-189. Print.

[19] R. Austin, *Unmanned Aircraft Systems: UAVs Design, Development, and Deployment*. Wiltshire, UK: John, 2010.

[20] "U.S. Air Force Fact Sheet: MQ-1B Predator." Air Combat Command.

[21] "U.S. Air Force Fact Sheet: MQ-9 Reaper." Air Combat Command.

[22] "U.S. Air Force Fact Sheet: RQ-4 Global Hawk." Air Combat Command.

[23] AFCESA/CEO, "Engineering Technical Letter 09-1: Airfield Planning and Design Criteria for Unmanned Aircraft Systems." Air Force Civil Engineer Support Agency, 28-Sep-2009.

[24] M. Sadraey, "Wing Design," Sep-2012. [Online]. Available: http://faculty.dwc.edu/sadraey/Chapter%205.%20Wing%20Design.pdf.

[25] I. Abbott, A. von Doenhoff, and L. Stivers, "Summary of Airfoil Data," National Advisory Committee for Aeronautics, 824, 1945.

[26] D. Lednicer, "The Incomplete Guide to Airfoil Usage," *The Incomplete Guide to Airfoil Usage*, Sep-2010. [Online]. Available: http://www.ae.illinois.edu/m-selig/ads/aircraft.html. [Accessed: 13-Mar-2012].

[27] P. Svacek, M. Feistauer, and J. Horacek, "Numerical Simulation of Flow Induced Airfoil Vibrations with Large Amplitudes," *Journal of fluids and structures*, vol. 23, pp. 391–411, 2007.

[28] S. Mollahajloo and M. Rahimian, "Numerical Simulation of Flow Induced Vibration of a Two-Dimensional Airfoil," *AIP Conference Proceedings*, vol. 1168, no. 535, 2009.

[29] E. Sæta, "Design of Airfoil for Downwind Wind Turbine Rotor." Norwegian University of Science and Technology, Jun-2009.

[30] R. Craig, *Structural Dynamics: An Introduction to Computer Methods*. New York, NY: John Wiley & Sons, 1981.

[31] B. Donaldson, *Introduction to Structural Dynamics*. New York, NY: Cambridge University Press, 2006.

[32] J. Wright and J. Cooper, *Introduction to Aircraft Aeroelasticity and Loads*. Reston, VA: AIAA, 2007.

[33] M. Goland, "The Flutter of a Uniform Cantilever Wing," *Journal of Applied Mechanics*, vol. 12, no. 4, p. A197–A208, 1945.

[34] T. Yechout, S. Morris, D. Bossert, and W. Hallgren, *Introduction to Aircraft Flight Mechanics*. Re: AIAA, 2003.

[35] J. Katz and A. Plotkin, *Low-Speed Aerodynamics*, 2nd ed. Cambridge, UK: Cambridge University Press, 2001.

[36] T. Theodorsen, "General Theory of Aerodynamic Instability and the Mechanism of Flutter," NACA Report 496, 1935.

[37] H. Wagner, "Uber die Entstehung des dynamischen Auftriebes von Tragflugeln," *Angewandte Mathematik und Mechanick*, vol. 5, no. 1, pp. 17–35, 1925.

[38] J. G. Leishman, *Principles of Helicopter Aerodynamics*. Cambridge: Cambridge University Press, 2000.

[39] W. J. Cunningham, *Introduction to Nonlinear Analysis*. York, PA: McGraw-Hill, 1958.

[40] J. R. Dormand and P. J. Prince, "A Family of Embedded Runge-Kutta Formulae," *Journal of Computational and Applied Mathematics*, vol. 6, no. 1, pp. 19–26, 1980.

[41] D. Houcque, "Applications of MATLAB: Ordinary Differential Equations (ODE)." Northwestern University.

[42] B. Tongue, *Principles of Vibration*. New York, NY: Oxford University Press, 1996.

[43] J. Thomas, E. Dowell, and K. Hall, "Nonlinear Inviscid Aerodynamic Effects on Transonic Divergence, Flutter, and Limit-Cycle Oscillations," *AIAA Journal*, vol. 40, no. 4, p. 638–46, Apr. 2002.

[44] T. Ueda and E. H. Dowell, "Flutter Analysis Using Nonlinear Aerodynamic Forces," *Journal*, vol. 21, no. 2, p. 101–9, 1984.

[45] R. Mickens, *Truly Nonlinear Oscillations*. Singapore: B & JO Enterprise, 2010.

[46] P.-T. Spanos and W. D. Iwan, "Harmonic Analysis of Dynamic Systems With Nonsymmetric Nonlinearities," *Journal of Dynamic Systems, Measurement, and Control*, vol. 101, p. 31–6, Mar. 1979.

[47] J. Holmes, *Wind Loading of Structures*. New York, NY: Spon Press, 2001.

[48] F. Hoblit, *Gust Loads on Aircraft*. Washington, D.C.: AIAA, 1988.

[49] "Von Karman Wind Turbulence Model." MathWorks.

[50] "U.S. Military Specification," MIL-F-8785C, Nov. 1980.

[51] "U.S. Military Handbook," MIL-HDBK-1797, Dec. 1997.

[52] T. S. Beddoes, "A Synthesis of Unsteady Aerodynamic Effects Including Stall Hysteresis," *Vertica*, vol. 1, pp. 113–123, 1976.

[53] J. G. Leishman and T. S. Beddoes, "A Generalized Model for Airfoil Unsteady Aerodynamic Behavior and Dynamic Stall Using the Indicial Method," presented at the 42nd Annual Forum of the American Helicopter Society, Washington, D.C., 1986, pp. 243–265.

[54] K. W. McAlister, O. Lambert, and D. Petot, "Application of the ONERA Model of Dynamic Stall," NASA, NASA Technical Paper 2399, Nov. 1984.

[55] J. B. Roberts and P. D. Spanos, *Random Vibration and Statistical Linearization*. West Sussex, England: John Wiley & Sons, 1990.

[56]   P. D. Spanos and J. E. Hansen, "Linear Prediction Theory for Digital Simulation of Sea Waves," *Journal of Energy Resources*, vol. 103, pp. 243–249, 1981.

[57]   P. D. Spanos, "ARMA Algorithms for Ocean Wave Modeling," *Transactions of ASME*, vol. 105, pp. 300–309, Sep. 1983.